

Sensitivity of salt intrusion to estuary-scale changes

A systematic modelling study towards nature-based mitigation measures

Hendrickx, Gijs G.; Kranenburg, Wouter M.; Antolínez, José A.A.; Huismans, Ymkje; Aarninkhof, Stefan G.J.; Herman, Peter M.J.

DOI

[10.1016/j.ecss.2023.108564](https://doi.org/10.1016/j.ecss.2023.108564)

Publication date

2023

Document Version

Final published version

Published in

Estuarine, Coastal and Shelf Science

Citation (APA)

Hendrickx, G. G., Kranenburg, W. M., Antolínez, J. A. A., Huismans, Y., Aarninkhof, S. G. J., & Herman, P. M. J. (2023). Sensitivity of salt intrusion to estuary-scale changes: A systematic modelling study towards nature-based mitigation measures. *Estuarine, Coastal and Shelf Science*, 295, Article 108564. <https://doi.org/10.1016/j.ecss.2023.108564>

Important note

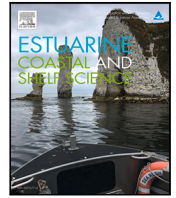
To cite this publication, please use the final published version (if applicable). Please check the document version above.

Copyright

Other than for strictly personal use, it is not permitted to download, forward or distribute the text or part of it, without the consent of the author(s) and/or copyright holder(s), unless the work is under an open content license such as Creative Commons.

Takedown policy

Please contact us and provide details if you believe this document breaches copyrights. We will remove access to the work immediately and investigate your claim.



Sensitivity of salt intrusion to estuary-scale changes: A systematic modelling study towards nature-based mitigation measures

Gijs G. Hendrickx^{a,*}, Wouter M. Kranenburg^{a,b}, José A.A. Antolínez^a, Ymkje Huismans^{a,b}, Stefan G.J. Aarninkhof^a, Peter M.J. Herman^{a,b}

^a Department of Hydraulic Engineering, Delft University of Technology, Delft, The Netherlands

^b Unit Marine and Coastal Systems, Deltares, Delft, The Netherlands

ARTICLE INFO

Keywords:

Estuaries
Nature-based solutions
Salt intrusion
Sensitivity analysis
3D modelling

ABSTRACT

Estuaries are among the most densely populated and heavily utilised regions in the world, where crucial functions – e.g., freshwater availability and water safety – strongly relate to the natural dynamics of the system. When developing nature-based solutions to safeguard these essential functions, a thorough understanding of estuarine dynamics is required. This study describes an elaborate sensitivity analysis on the salt intrusion length using an idealised estuary, which is parametrically designed using key estuary-scale parameters – e.g., river discharge and tidal flats – to cover a wide range of estuary classes. We were able to systematically investigate such a wide range of estuary classes due to the combination of (1) state-of-the-art hydrodynamic modelling software, (2) high performance computing, and (3) reduction and analysis techniques using machine learning. The results show that the extent of the estuarine salt intrusion length is largely determined by four estuarine features: (1) river discharge; (2) cross-sectional area (especially water depth); (3) tidal damping/amplification; and (4) tidal asymmetry. In general, the salt intrusion length shows clear correlations with (a combination of) estuary-scale parameters, which all put an upper limit on the salt intrusion length. These relations provide crucial insights for successful development of nature-based solutions to mitigate salt intrusion in estuarine environments.

1. Introduction

Around the world, estuarine regions are among the most populated areas with approximately 1.2 billion people living within 100 km from the coastline (Small and Nicholls, 2003). These regions heavily rely on the supply of freshwater from the river systems, which can salinise due to their closeness to the sea (Costall et al., 2018). Currently, water stress – i.e., the unavailability of freshwater – is a global issue (Mekonnen and Hoekstra, 2016), and it is most profound in these coastal regions (Wada et al., 2011). Unsustainable groundwater abstraction is already occurring worldwide (Wada et al., 2010), which is a clear indicator of the current water stress.

The severity of water stress will likely increase due to climate change (e.g., Distefano and Kelly, 2017; Veldkamp et al., 2015) by means of (relative) sea level rise and increased frequency and duration of droughts. Both will enhance the salt intrusion and so further reduce the availability of freshwater in estuarine regions. In addition, while the supply of freshwater is threatened due to climate change, the demand will grow due to the expected increase in population density in coastal regions (Small and Nicholls, 2003).

Freshwater challenges due to salt intrusion via surface water can be mitigated by means of hard measures, such as dams and locks. However, these measures have many negative side-effects, e.g., blockage of the river flow and disturbance of the environment. This has resulted in the motivation for this study: Are nature-based solutions to mitigate salt intrusion a viable substitute for their hard counterparts?

Nature-based solutions follow the *Building with Nature*-approach (de Vriend et al., 2015) in which there is special attention for the system as a whole. Note that such a system extends beyond the physical domain as it also includes the ecological and socio-economic perspectives (van Slobbe et al., 2013).

Because nature-based solutions attempt to utilise natural processes, they are commonly more resilient to changes in the boundary conditions and can adapt along those changes (Borsje et al., 2011). There are, of course, limitations to the adaptability of a nature-based solution. Nonetheless, this adaptability is of increasing importance due to climate change. Furthermore, including ecological processes that are accommodated by these natural processes also creates additional value from both socio-economic and ecological perspectives (e.g., Scheres and

* Corresponding author.

E-mail address: G.G.Hendrickx@tudelft.nl (G.G. Hendrickx).

Schüttrumpf, 2019; van Wesenbeeck et al., 2014). Therefore, they accommodate for a sustainable solution on the long term. The application of the *Building with Nature*-approach on the topic of salt intrusion has not yet been studied so far, which is the focus point of this study.

The first step of the *Building with Nature*-approach is to understand the system (de Vriend et al., 2015); in this study, this is the estuarine system. There have been significant developments in attaining knowledge and expertise in understanding the salt intrusion in estuaries (see reviews by MacCready and Geyer, 2010; Geyer and MacCready, 2014). For example, many studies have highlighted the importance of the water depth (e.g., Chant et al., 2018; Ralston and Geyer, 2019) and the river discharge (e.g., Gong and Shen, 2011; Lerczak et al., 2009) on the salt intrusion length. In addition to these, many geometric features have been shown to influence the salt intrusion (Veerapaga et al., 2020), such as tidal flats (Lyu and Zhu, 2019; Zhou et al., 2020). The literature about salt intrusion in estuaries is vast of which a very comprehensive review is presented in Section 2.

Due to the complexity associated with salt intrusion processes, state-of-the-art, computationally expensive models are required to assess these processes with sufficient detail. This often yields limitations in terms of number of simulations that can be achieved (e.g., Ralston et al., 2010; Warner et al., 2005). Alternately, simplified models are used to explore a broader range of input conditions and/or estuary geometries (e.g., Dijkstra and Schuttelaars, 2021; Kuijper and van Rijn, 2011; MacCready, 1999). Although these studies provide valuable insights into the estuarine processes, they may easily overlook important interactions in a system determined by a highly multidimensional parameter space.

The aim of this paper is to systematically assess the sensitivity of salt intrusion length to changes in system characteristics. Thereby we address the research question how sensitive salt intrusion length is to changes in the forcing conditions and geomorphological features of an estuary. These relations are explored by means of a sensitivity analysis with the aim to enable the evaluation of nature-based solutions to mitigate salt intrusion. Subsequently, this study includes a first overview of the translation from the sensitivity analysis to the validation of hypothesised potential nature-based solutions to mitigate salt intrusion. These potential nature-based solutions are based on literature – reviewed in Section 2 – and function as design directions.

To answer the research question and evaluate subsequent hypotheses, Section 2 presents a literature review from which the hypotheses are drawn. The methodology used to conduct the sensitivity analysis is presented in Section 3. The results of the sensitivity analysis are presented in Section 4. Section 5 further discusses the results and evaluates the posed hypotheses of Section 2. Finally, Section 6 draws conclusions on the estuarine response to various modifications with a special focus on the hypothesised nature-based solutions.

2. Estuarine salt dynamics

Estuarine salt intrusion is the result of a continuously changing competition between inward and outward transport mechanisms. The main driver of the outward transport is the river discharge, which flushes the system and advects salt seaward. Inward transporting mechanisms can be split in tide-averaged shear and tidal flow related mechanisms. Tide-averaged shear is generally referred to as estuarine circulation, which can be decomposed into various driving mechanisms (Burchard and Hetland, 2010), most notably gravitational circulation (e.g., Hansen and Rattray, 1965) and tidal straining (e.g., Jay and Musiak, 1994). An example of the second category is tidal trapping (Fischer et al., 1979), where the timing of the release of salt water that has come in during flood but was temporarily stored, e.g., in side-channels or on tidal flats, causes a net influx of salt (e.g., Garcia et al., 2021; Zhou et al., 2020).

The strength of the various transport mechanisms is predominantly determined by the hydrodynamic forcing conditions and system geomorphology. In estuaries, the main hydrodynamic forcing consists of

the tide and the river discharge (e.g., Geyer and MacCready, 2014). During flood tide, salt water is pushed into the estuary, while introducing energy to mix the water column (e.g., Simpson et al., 1990). In contrast, the river discharge pushes the salt water seaward and provides buoyancy by the supply of freshwater (e.g., Lerczak et al., 2009). Thus, both forcing terms have enhancing and reducing effects on the salt intrusion.

In addition to tidal forcing and river discharge, other key coastal processes modify the salt intrusion length. For example, the occurrence of strong onshore directed winds and the resulting storm surge enhance the salt intrusion in an estuary (Kranenburg et al., 2022). However, storms have also shown to reduce the estuarine salt intrusion (Geyer, 1997) in which the wind direction plays an important role.

In essence, the estuary's geomorphology largely determines how the estuary responds to these forcing conditions and can even modify the forcing to a certain level. In the end, the balance between the forcing terms determines the salt intrusion length, where the estuarine geomorphological features modify the arena in which this battle is played out. In this study, we focus on the key geomorphological features listed in Table 1.

The water depth of the estuary has long been known to be of great influence on the salt intrusion (e.g., Hansen and Rattray, 1965): An increased water depth reduces the vertical mixing as the vertical shear velocity becomes smaller (Chant et al., 2018; MacCready and Geyer, 2010). Furthermore, the fluvial flow velocity reduces as the cross-sectional area increases, which is similarly affected by the width.

In addition to these two basic geometric characteristics, the balance between width convergence and bottom friction determines whether the tidal signal is amplified or damped (e.g., Savenije and Veling, 2005; van Rijn, 2011): Convergence causes tidal amplification, while bottom friction results in tidal damping. As the tide is one of the main forcing conditions, these two geometric features indirectly modify the salt intrusion length by modifying the tidal wave.

Tidal asymmetry plays an important role in the salt intrusion, where an ebb-dominant system reduces the salt intrusion (Pein et al., 2018; Cheng et al., 2013) by stimulating a two-layered flow opposing the gravitational circulation (Cheng et al., 2010; Stacey et al., 2008). Ebb-dominance in an estuary can be enhanced by (1) introducing tidal flats (Friedrichs and Aubrey, 1988); (2) reducing the ratio of the tidal range over the water depth (Friedrichs and Madsen, 1992); and/or (3) increase the river discharge relative to the tidal flux (Nidziko and Ralston, 2012).

At last, two geometric features enhancing lateral mixing are: (1) lateral depth variation, and (2) meandering (Burchard et al., 2011; Lerczak and Geyer, 2004; Pein et al., 2018). The presence of lateral circulation patterns on their own reduces the salt intrusion by reducing the forward momentum. The lateral circulation pattern originates from laterally directed momentum, which has to draw from the forward momentum due to the conservation of momentum. Despite both a lateral depth variation and meandering promoting the formation of lateral circulation patterns, their net effects on salt intrusion are opposite; lateral depth variation enhances the salt intrusion, while meandering reduces the intrusion.

The lateral depth variation is often represented by a cross-sectional curvature of the bottom profile (e.g., Burchard et al., 2011; Lerczak and Geyer, 2004). The flow velocity in the centre of the channel is larger due to this bottom curvature, which enhances the salt transport in the centre (Burchard et al., 2011; Lerczak and Geyer, 2004). Although the resulting lateral density differences do create lateral circulation patterns (i.e., differential advection; Nunes and Simpson, 1985), this process generally enhances the longitudinal dispersion of salt, i.e., the salt intrusion. The salt moves faster landward during flood where it is pushed to the sides due to the lateral circulation, but is afterwards not completely flushed out by the ebb flow which is also faster in the centre, while the salt has partly moved to the sides of the channel (Burchard et al., 2011).

Conversely, meandering within the reach of salt intrusion can reduce its landward extent (Pein et al., 2018). The lateral mixing due to the secondary circulation initiated by bends in the estuary reduces the propagation of salt water upstream and so reduces the salt intrusion.

On the basis of the aforementioned processes and studies, we hypothesise six design directions for nature-based solutions to mitigate salt intrusion:

1. reduced cross-section;
2. increased bottom friction;
3. enlarged tidal flats;
4. reduced lateral depth variation;
5. increased meandering;
6. managed river discharge.

The type of estuary is expected to influence the salt intrusion, as different physical processes are dominant per type. In this study, we use the classification by Geyer and MacCready (2014), which divides estuaries into eight classes based on two non-dimensional parameters: (1) the mixing parameter, M (Eq. (1)); and (2) the freshwater Froude number, Fr_f (Eq. (2)). Their definitions are presented below (Geyer and MacCready, 2014):

$$M = \sqrt{\frac{c_f u_t^2}{\omega_t N d_c^2}} \quad (1)$$

where c_f is the non-dimensional friction coefficient [-]; u_t the tidal flow velocity [ms^{-1}]; ω_t the tidal frequency [s^{-1}]; N the buoyancy frequency [s^{-1}]; and d_c the (channel) depth [m]. These variables are defined as functions of the input space (Table 1) as follows:

$$c_f = \frac{g n_c^2}{d_c^{1/3}}$$

$$u_t = \frac{1}{2\sqrt{2}} \sqrt{\frac{g}{d_c}} a$$

$$N = \sqrt{\frac{g\beta s_0}{d_c}}$$

where g is the gravitational acceleration [$g = 9.81 \text{ ms}^{-2}$]; n_c the Manning's n [$\text{s m}^{-1/3}$]; a the tidal range [m]; β the haline contraction coefficient [$\beta = 7.6 \times 10^{-4} \text{ psu}^{-1}$]; and s_0 the oceanic salinity [$s_0 = 30 \text{ psu}$].

$$Fr_f = \frac{Q}{W_c d_c c_i} \quad (2)$$

where Q is the river discharge [m^3s^{-1}]; W_c the (channel) width [m]; and c_i the maximum frontal propagation speed, or internal celerity [ms^{-1}]:

$$c_i = \sqrt{d_c g \beta s_0}$$

The aforementioned dominant roles of the tide and the river discharge are encapsulated in these non-dimensional parameters, where the mixing parameter (M) reflects the tidal energy, and the freshwater Froude number (Fr_f) the fluvial energy input.

3. Method

To perform the sensitivity analysis, we implemented a simulation strategy enabled by machine learning techniques. The use of adaptive sampling allowed the use of computationally expensive models for exploring the salt intrusion length for various estuarine layouts while remaining computationally feasible. This strategy required the description of the input space (Section 3.1) used by various machine learning techniques to draw the “most valuable samples” following an adaptive sampling approach (Section 3.2). These selected samples determined the layout of an idealised estuary, which was subsequently simulated using a state-of-the-art hydrodynamic model (Section 3.3). As

Table 1

Input parameters including their ranges and units. The values are largely based on datasets included in Dronkers (2017), Leuven et al. (2019) and Savenije et al. (2008).

	Parameter	Symbol	Range		Unit
Forcing	Tidal range	a	1.0	5.0	m
	Storm surge level	η_s	0.0	2.0	m
	River discharge	Q	100	16,000	$\text{m}^3 \text{ s}^{-1}$
Geomorphology	Channel depth	d_c	5.0	25.0	m
	Channel width	W_c	500	3,000	m
	Channel friction	n_c	0.01	0.05	$\text{s m}^{-1/3}$
	Flat depth ratio ^a	r_d	-1	1	-
	Flat width	W_f	0	3,000	m
	Flat friction	n_f	0.02	0.05	$\text{s m}^{-1/3}$
	Convergence	γ	2.5	40	$\times 10^{-5} \text{ m}^{-1}$
	Bottom curvature	κ_c	0.0	6.0	$\times 10^{-5} \text{ m}^{-1}$
Meander amplitude	A_m	0	6	km	
Meander length	L_m	0	100	km	

^a The flat depth is defined as the product of the flat depth ratio and the tidal range: $d_f = \frac{1}{2} r_d a$. Thereby ensuring that the tidal flats are at all times exposed and flooded during a tidal cycle, which is inherent to a tidal flat.

the simulated samples do not form clear planes through the explored 13-dimensional space, various techniques have been used to post-process and analyse the output data (Section 3.4). The implemented simulation strategy is discussed in detail in Hendrickx et al. (2023) and this section is a brief overview of their work.

3.1. Input space

Based on the aforementioned literature on key estuarine characteristics, thirteen input parameters have been selected to include in the sensitivity analysis: three hydrodynamic forcing conditions, and ten geometric features. The definitions of the input parameters are presented in Table 1 (modified from Hendrickx et al., 2023) and visualised by the schematic overview of the parametric design in Fig. 1.

The results from the many estuarine layouts that follow as a combination of the input parameters presented in Table 1 (and discussed in Section 2) allow the investigation of the hypotheses presented in Section 2 representing the worldwide variations in estuaries. The parametric design is a simplification of real-life estuaries, which allows the analysis to focus on the relevant estuary-scale parameters and the differences in output they enforce.

3.2. Simulation strategy

For a sensitivity analysis, the number of simulations required for robust results increases rapidly with the number of input parameters; the thirteen input parameters considered in this study would require at least 3^{13} ($\approx 1.6 \times 10^6$) simulations (Wang et al., 2020), which would cover three values per input parameter. As a computationally expensive hydrodynamic model is used for every single simulation (see Section 3.3), this number of simulations becomes computationally infeasible to execute.

Therefore, machine learning techniques have been adopted to optimise the selection procedure of forcing conditions and geomorphological features for simulation (Hendrickx et al., 2023). The number of simulations is drastically reduced to approximately 1250 simulations while still being able to gain insights into the response of the system to the parameter variations.

The core of the used simulation strategy follows an adaptive sequential design, where the configuration of the next simulation is based on the output of completed simulations instead of prescribing all model configurations *a priori*. The new set of input parameters are chosen based on the method developed by Gramacy and Lee (2009) in which a treed Gaussian process, limiting linear model determines new samples by maximising the expected entropy. Due to this adaptive sampling

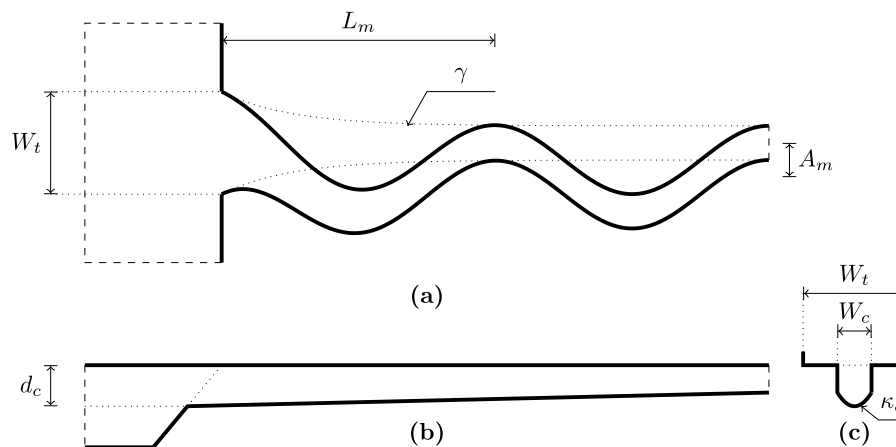


Fig. 1. Parametric model design. (a) Plan view; (b) longitudinal cross-section; and (c) lateral cross-section. The meaning of the symbols are presented in Table 1, except for W_t : This is the total width, i.e., $W_t = W_c + W_f$.

technique, the choice to sample an estuary layout is based on the expected added information it will provide; translated to this study, “information” can be expressed as “better understanding the estuarine response.”

This adaptive simulation strategy was initiated by an initial batch of 100 samples for which the maximum dissimilarity algorithm (Kennard and Stone, 1969) was used to explore the outskirts of the input space. As the algorithm’s name suggests, it selects the most dissimilar samples in a given dataset based on their Euclidean distance (the dataset is normalised such that it forms a unit hypercube, i.e., *min-max* scaling). Subsequently, the adaptive sequential design contributed approximately 1100 samples to the dataset.

The resulting dataset of approximately 1200 simulations was used to train a neural network. Together with a genetic algorithm, this neural network was used to predict extremes in the output space, which were subsequently simulated with the hydrodynamic model as well. In this way, 50 additional simulations are executed creating a dataset of approximately 1250 simulations that has been used for the analysis presented in this paper.

3.3. Hydrodynamic model

The hydrodynamic modelling software used for the simulations is Delft3D Flexible Mesh (Kernkamp et al., 2011), which assumes hydrostatic pressure and solves the Reynolds-averaged Navier–Stokes equations using a $k-\epsilon$ turbulence closure. This state-of-the-art hydrodynamic model is used to enable relaxation of most assumptions that restrict the application of many other, simpler models. However, the use of such a process-based model comes at a higher computational cost, which motivated the aforementioned simulation strategy (Section 3.2; Hendrickx et al., 2023).

For this exploratory study, an estuary with idealised geomorphology is used as basis for the parametric model design in which all thirteen input parameters are reflected (see Table 1 and Fig. 1). The domain of the model consists of two parts: (1) the shelf, and (2) the estuary. The shelf domain is largely constant for all model configurations but the estuary domain changes substantially based on the provided geomorphological features; e.g., the width of the estuary changes between different simulations.

The definitions of the boundary conditions are kept relatively simple: The tide at sea is fully represented with a tidal period of twelve hours, similar to an S_2 -tide, and there is a constant river discharge. A storm surge level is superimposed on the tidal water levels. The storm surge follows a triangular profile over time from 0 m to its maximum (i.e., η_s) after twelve hours, subsequently reducing back to 0 m (following the same approach as Perk et al., 2019). Furthermore,

the upstream channel dimensions are a power function of the river discharge (based on Leuven et al., 2018b) to ensure reasonable flow conditions upstream.

The shelf model domain is a square of 30×30 km. Its grid resolution increases from the seaward boundary to the estuary mouth, with cell sizes decreasing from 1000×1000 m to 62.5×62.5 m. The estuarine domain has a length of 200 km and a varying width. The grid resolution decreases further upstream, with cell sizes increasing from 62.5×62.5 m at the estuary mouth to $\leq 250 \times 1000$ m at the upstream boundary; due to the convergence of the estuary, the grid cells are reduced in width.

The extent of the high resolution in the estuary domain – i.e., the grid resolution of 62.5×62.5 m – is determined based on an estimated salt intrusion length plus half the tidal excursion; both are determined analytically following Savenije (1989, 1993). The transition between different grid resolutions is facilitated by using triangular grid cells.

The models have been discretised vertically by twenty σ -layers. We are aware that Z -layers are preferred, especially for modelling of salt wedges (Stelling and Van Kester, 1994). However, σ -layers have been used to accommodate for the large range of water depths considered in this study (Table 1).

The initial salt concentration in the hydrodynamic model is based on an analytical model (Savenije, 1989, 1993) to reduce the spin-up time. To ensure that the results are not influenced by the initial conditions, the first eight days of the simulation are considered part of the spin-up time. The model data of the ninth simulated day is used for subsequent analyses. One day of data suffices, as the tidal forcing consists of only one tidal component, which occurs exactly twice per day due to its 12-hour period. Therefore, there are no neap-spring cycles or alike in the tidal forcing, which would require a longer simulation period.

The simulations were executed on a supercomputer. A single Delft3D Flexible Mesh simulation was run in parallel on 32 cores and has an execution time between fifteen minutes and five days—largely influenced by the geomorphology of the estuary, and thus the grid size.

3.4. Post-processing

The output of the simulations is expressed in terms of the salt intrusion length. This length is defined as the distance from the mouth of the estuary at which the depth- and tide-averaged salinity equals 1 psu. Because the salinity data is retrieved in a discrete manner from the hydrodynamic model’s numerical grid, the salinity is linearly interpolated between data points to determine the salt intrusion length.

As the used simulation strategy results in a reduced dataset (see Section 3.2), standard quantification methods for sensitivity analyses cannot be used (such as Saltelli et al., 2006; Sobol’, 2001; Wang et al., 2020). Instead, we apply a regression analysis. A multiple regression

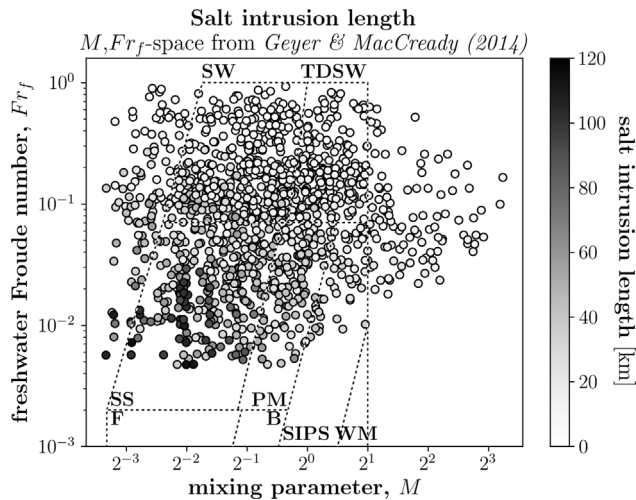


Fig. 2. Simulated estuary configurations overlaying the classification diagram by Geyer and MacCready (2014). The data is colour-coded with the salt intrusion length. The abbreviations refer to the estuary classes: SW, salt wedge; TDSW, time-dependent salt wedge; SS, strongly stratified; PM, partially mixed; F, fjord; B, bay; SIPS, strain-induced periodic stratification; WM, well-mixed.

model and neural network are fitted with the input and output data to determine the underlying relations between the input parameters and the output variable, i.e., salt intrusion length.

Although the predictive capability of a neural network is generally superior to the multiple regression model for highly dimensional input spaces, the neural network is often perceived as a *black box* as it is hard to retrieve what is exactly going on internally. The multiple regression model, on the other hand, is valuable precisely due to its transparency, where the over-fitted regression coefficients function as a quantification of the sensitivity of the salt intrusion length to the input parameters. Consequently, both regression methods are used in this study: The multiple regression model and its regression coefficients to gain insights into the response of the salt intrusion length to the 13-dimensional input (Section 3.4.1); and the neural network as predictive tool allowing to explore the hypothesised nature-based solutions to mitigate salt intrusion (Section 3.4.2).

3.4.1. Multiple regression model

The implemented regression model is defined as:

$$\hat{y} = \underbrace{C}_{\text{constant}} + \underbrace{\sum_{i=1}^P c_i x_i}_{\text{linear}} + \underbrace{\sum_{i \leq j}^P c_{i,j} x_i x_j}_{\text{nonlinear}} \quad (3)$$

where c_i and $c_{i,j}$ are the regression coefficients; x_i (or x_j) is the input parameter i (or j); and P the number of parameters ($P = 13$).

The regression model is over-fitted to the data by optimising the values of the regression coefficients to provide the best fit. The over-fitting causes the regression model unsuitable for predictive purposes but by doing so, provides insights into the data it represents.

The regression coefficients provide a quantification of the sensitivity of the output to the input parameters: The larger the absolute value of a regression coefficient, the larger the connectivity between the input parameter(s) and the output data. The level of connectivity is a quantification of the sensitivity of the output to the input parameter(s). The sign of the coefficient's value represents a positive (+) or a negative (-) relation between the input parameter(s) and the output, i.e., the salt intrusion length.

Note that the input data has to be normalised for this approach to work properly, as otherwise the order of magnitude of the input values determine the order of magnitude of the regression coefficients. This normalisation follows the *zero mean, unit variance*-approach.

3.4.2. Neural network

The neural network used contains three hidden layers of 50 nodes each. Over-fitting the neural network has been prevented by subdividing the output data in a training and testing (or validation) dataset (80% and 20%, resp.). While training, the neural network only uses the training data, while the testing data was used to validate the predictive power of the neural network. The best fit is reached when the neural network shows the smallest error on the testing data.

4. Results

For the presentation of the results, the over-fitted regression model as well as the neural network are used. Both models show a great fit with the data: The regression model has an $R^2 = 0.9581$, and the neural network linearly correlates even better, with $R^2 = 0.9912$. The R^2 -score is the coefficient of determination for which $R^2 = 1.0$ is the best possible score and negative values are possible, reflecting increasingly worse performing models. These great fits have been achieved while the dataset covers a multitude of estuary classes as defined by Geyer and MacCready (2014), which is illustrated in Fig. 2.

4.1. Upper limits of salt intrusion length

The projection of the salt intrusion length on the M, Fr_f -space presented in Fig. 2 shows a gradient in the salt intrusion length (Fig. 2) in response to both the mixing parameter (M , Eq. (1)) and the freshwater Froude number (Fr_f , Eq. (2)). This indicates that the salt intrusion length is generally the largest for *strongly stratified* estuaries in comparison to the other estuary classes.

As we are comparing non-dimensional numbers with the salt intrusion length – a dimensional variable – it is important to stress that these results hold for the ranges used in this study (Table 1). Although the explored input space is representative for estuaries worldwide, these results do not exclude the theoretical possibility of large salt intrusion lengths for large values of the freshwater Froude number and/or mixing parameter.

In Fig. 2, the salt intrusion length reduces for increasing values of the mixing parameter and/or freshwater Froude number. This implies that the five input parameters – out of the thirteen – that are reflected by these non-dimensional numbers largely explain the variability in the salt intrusion length. The mixing parameter increases for (1) increasing tidal range, $M \propto a$; (2) decreasing channel depth, $M \propto d_c^{-17/12}$; and (3) increasing (channel) friction, $M \propto n_c$. The freshwater Froude number increases for (1) increasing river discharge, $Fr_f \propto Q$; (2) decreasing channel depth, $Fr_f \propto d_c^{-3/2}$; and (3) decreasing channel width, $Fr_f \propto W_c^{-1}$.

The variability in salt intrusion length visible in Fig. 2 suggests that the salt intrusion can be large, unless a limiting factor is imposed. One such limiting factor is the channel depth, as shown in Fig. 3a: A smaller channel depth enforces a reduction in the salt intrusion length. A larger channel depth does not necessarily result in a larger salt intrusion length, but is an enabler of large salt intrusion lengths.

Similar relations between the salt intrusion length and other input parameters exist (see *Supplementary material*), most notably with the convergence (Fig. 3b). Although the M, Fr_f -space shows to be explain a large part of the variability in the salt intrusion length (Fig. 2), this study shows the additional relevance of other estuary-scale parameters such as the convergence (Fig. 3b).

4.2. Importance of input parameters

The multiple regression model is able to encapsulate most of the variations in the output as shown by the great fit with the data, while being a linear model (Eq. (3)).

The regression coefficients show the sensitivity of the output to changes of the input parameter(s) and are presented as a matrix in

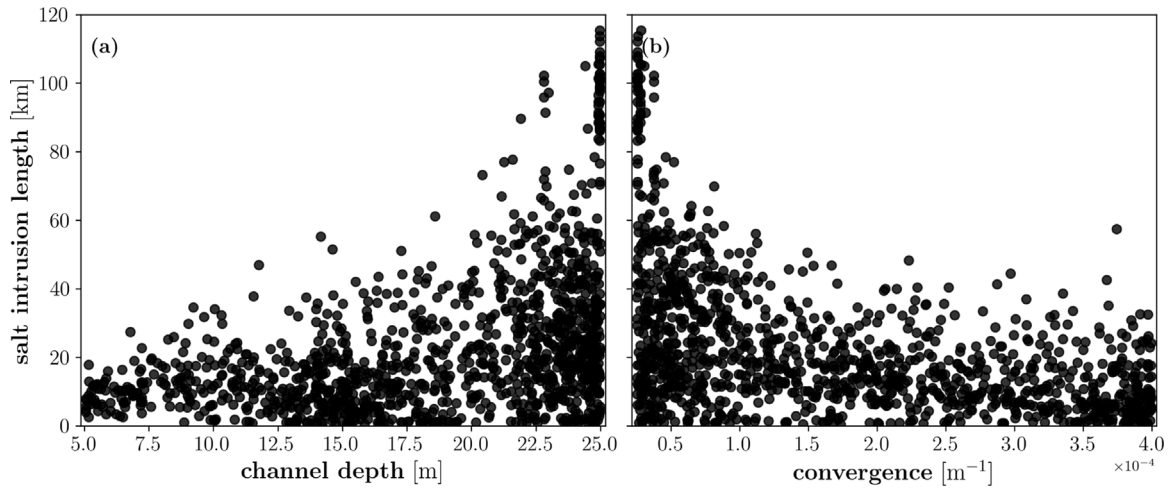


Fig. 3. Simulated salt intrusion length as function of (a) the channel depth, d_c , and (b) the convergence, γ .

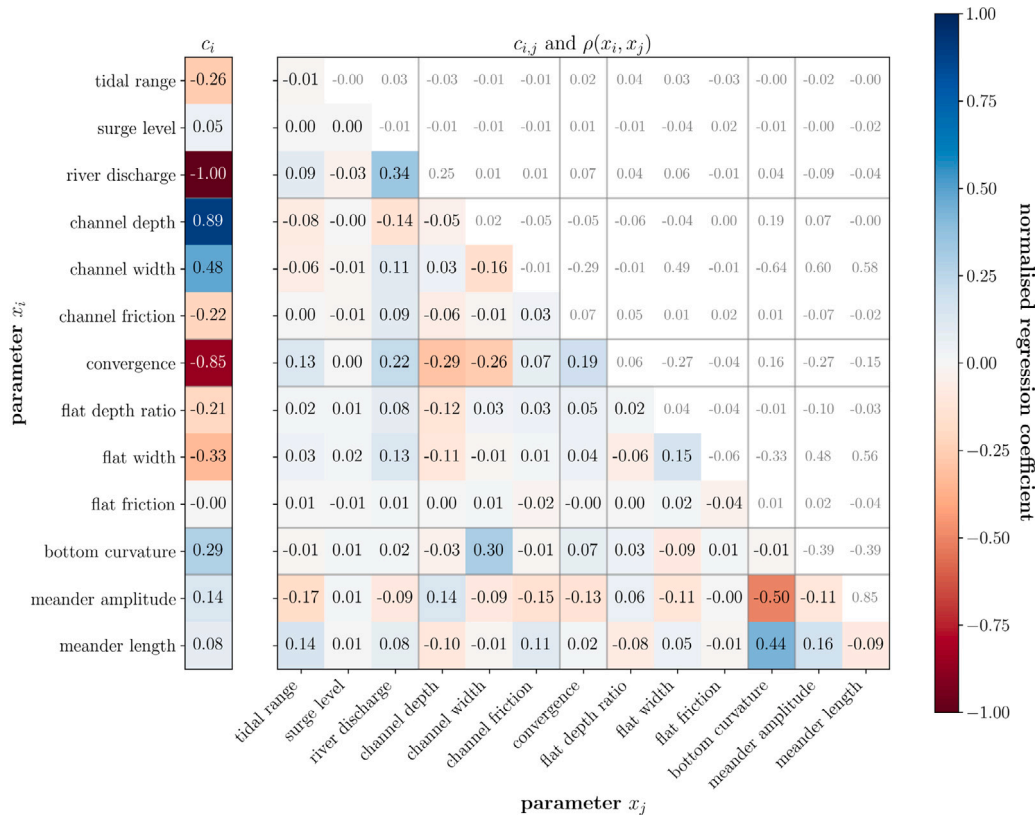


Fig. 4. System’s response represented by the (normalised) regression coefficients of the over-fitted regression model (Eq. (3)). The colour-coding represents the value of the regression coefficients, where a large absolute value is indicated by a darker colour and reflects a higher dependency of the output on the input parameter(s). Grey values represent the Pearson correlation coefficients, $\rho(x_i, x_j)$.

Fig. 4. The linear regression coefficients are presented in the most left column (titled c_i), and the quadratic and interaction terms are shown in the thirteen-by-thirteen matrix (titled $c_{i,j}$), which is symmetrical over its diagonal. The colour-coding represents the value of the regression coefficient, which is of interest for the sensitivity analysis. The grey-values in the matrix represent the Pearson correlation coefficients between parameters x_i and x_j : $\rho(x_i, x_j)$. The Pearson correlation coefficient has a range $\rho(x_i, x_j) \in [-1, +1]$ and a larger absolute value of the coefficient indicates a stronger correlation between the variables, where the sign is indicative for a positive (+) or negative (-) relation.

From this matrix follows that the salt intrusion length is highly dependent on the river discharge, channel depth, and convergence as

well as the interaction between the convergence with the river discharge, channel depth, and channel width. In addition, the interactions between the bottom curvature with the meandering specifications happen to be of substantial influence on the salt intrusion length. On the other hand, the friction of the tidal flats does not seem to influence the results. Fig. 4 also suggests that the surge level is irrelevant for the salt intrusion length, which is in contradiction with literature (Kranenburg et al., 2022). Although the presented salt intrusion length is taken as the tide averaged value, no substantial changes arise when considering the tidal maximum, which questions the implementation of the surge level in our parametric design.

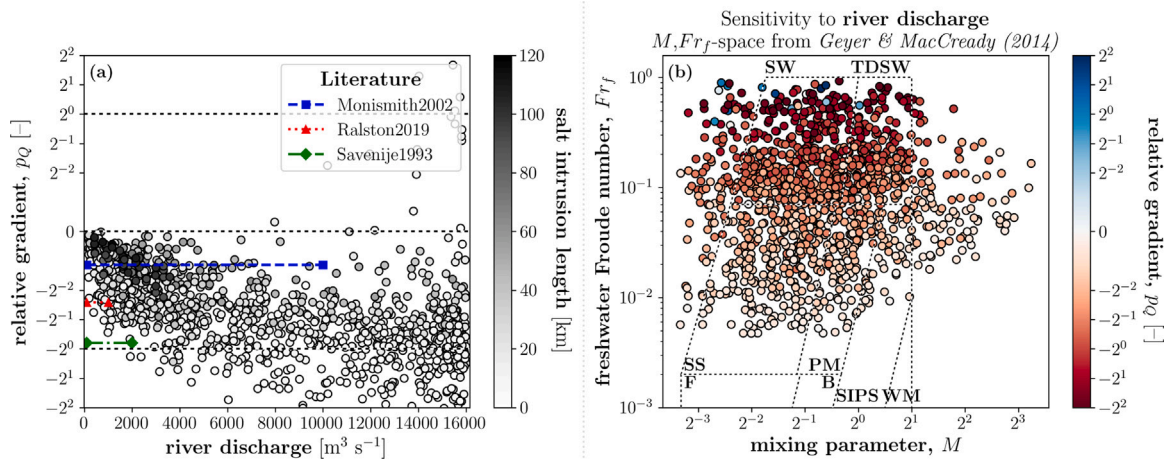


Fig. 5. The relative gradient in salt intrusion with respect to the river discharge, p_Q : (a) as function of the river discharge; (b) displayed on the M, Fr_f -space by Geyer and MacCready (2014) with the same class-labels as in Fig. 2. Data from literature displayed in (a): Monismith2002, Monismith et al. (2002); Ralston2019, Ralston and Geyer (2019); Savenije1993, Savenije (1993).

The nonzero correlations in Fig. 4 follow from the physical input check (see *Supplementary material*), and highlight potential false cause-and-effect relations. For example, the strong correlation between the meander amplitude and length ($\rho(A_m, L_m)$) is commonly seen in nature (e.g., Leuven et al., 2018a), and therefore, explicitly included in the physical input check. However, these meandering parameters are also both negatively correlated to the bottom curvature, while such a relation is not included in the physical check, and therefore, must follow via another input parameter—most likely the channel width. These correlations might explain the relatively high value of their first-order interaction regression coefficients seen in Fig. 4, c_{k_c, A_m} and c_{k_c, L_m} , as no clear direct relation between the salt intrusion length and the combination of these parameters can be seen in the raw data.

4.3. Salt intrusion gradients

The neural network is used to determine the partial gradients of the salt intrusion length with respect to one of the input parameters. These gradients are estimated using the forward Euler scheme:

$$\frac{\partial L_s}{\partial x_i} \approx \frac{L_s(\mathbf{x} + \mathbf{n}_i) - L_s(\mathbf{x})}{\Delta x_i} \quad (4)$$

where L_s is the salt intrusion length estimate [m]; x_i an input parameter; \mathbf{x} the vector of input values; \mathbf{n}_i the null-vector except the i th element, which equals Δx_i ; and Δx_i a very small step in the range of x_i :

$$\Delta x_i = \frac{\max\{x_i\} - \min\{x_i\}}{1000}$$

Note that for the determination of the gradients, the salt intrusion is estimated with the neural network both at \mathbf{x} and $\mathbf{x} + \mathbf{n}_i$. This minimises any bias of the neural network to be reflected in the salt intrusion gradients.

Overall, the computed absolute gradients in salt intrusion length are largest for larger values of the salt intrusion length; i.e., modifications of the estuarine system result in the largest changes in the salt intrusion when the salt intrusion length is already large.

However, this relation vanishes when the partial derivatives are normalised with the input parameter and salt intrusion length:

$$p_i = \frac{\partial L_s}{\partial x_i} \frac{x_i}{L_s} \quad (5)$$

where $\partial L_s / \partial x_i$ equals the partial derivative as stated in Eq. (4).

Eq. (5) reflects how much the salt intrusion length changes relatively compared to a relative change in the input parameter. Note that

this relative gradient p_i describes the power relation between the input parameter, x_i , and the salt intrusion length:

$$L_s \propto x_i^{p_i} \quad (6)$$

which is a commonly used form to describe the relation between estuarine characteristics and the salt intrusion length both in theoretical and empirical studies; e.g., the relation between the salt intrusion length and the river discharge is often described by such a power relation, where according to literature p_Q is in the range $-1/7$ to -1 (e.g., Monismith et al., 2002; Ralston and Geyer, 2019; Savenije, 1993). Fig. 5a conforms that p_Q varies around those values, and that the absolute value of p_Q increases with a higher river discharge.

Furthermore, the relative gradient, p_Q , shows a trend in the M, Fr_f -space (Fig. 5b) that may be a consequence of the freshwater Froude number definition (Eq. (2)), which is linearly related to the river discharge.

Fig. 6 presents relative gradients for the input parameters that are related to the other hypothesised nature-based solutions. (For similar figures for all input parameters, see the *Supplementary material*.) Where p_Q shows a dependence on the estuary class (Fig. 5), the relative gradient of the channel depth, p_{d_c} , shows less variability (Fig. 6a). The values of p_{d_c} might depart from the general range for very small values of the salt intrusion length ($L_s \rightarrow 0$), as with the outliers in p_Q (Fig. 5a); this is likely due to the definition of p_i (Eq. (5)) in which the derivative is divided by the salt intrusion length (L_s).

Both the relative gradients with respect to the channel depth (p_{d_c}) and channel friction (p_{n_c}) show the direct relevance of these input parameters as well as a gradient in their values in the M, Fr_f -space (Figs. 6a and b). The remainder of the input parameters that are associated with the hypothesised nature-based solutions show only a weak direct contribution to the salt intrusion length (Figs. 6c to f).

Note that the partial derivatives of the estuarine configurations with a larger salt intrusion must be considered with care—i.e., the data points located in the *strongly stratified*-class (Fig. 2). The implementation of the genetic algorithm to “find” these extremes results in limited variations in certain input parameters, which complicates the determination of a reliable partial derivative to these input parameters for such extremes in the output.

Furthermore, the relative gradient tends to be more sensitive to minor errors in the predictive power of the neural network for small values of the salt intrusion length, as these errors are relatively larger—especially for salt intrusion lengths near zero, where also a sign-change might occur.

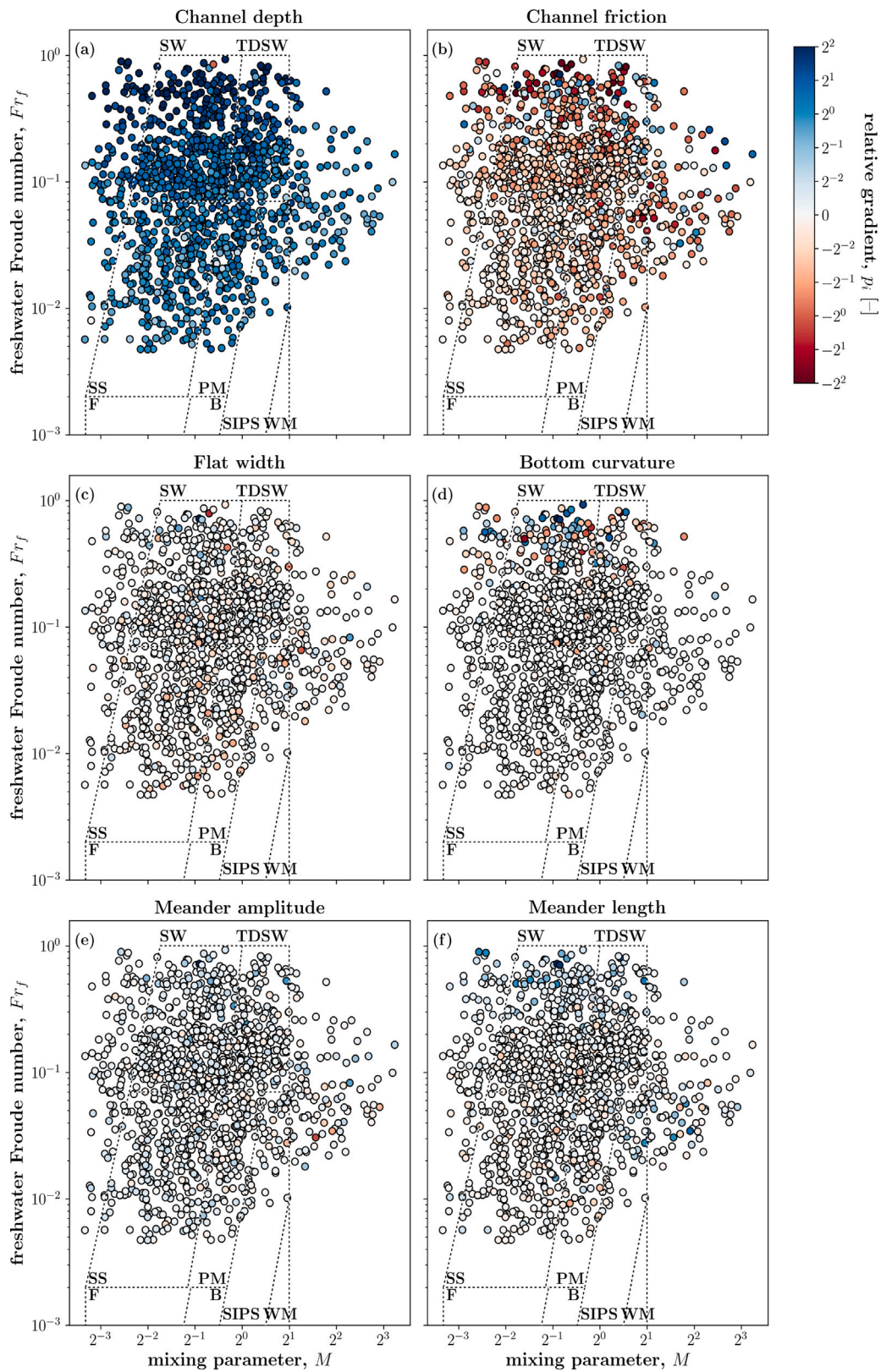


Fig. 6. Estimates of the relative gradient in salt intrusion with respect to six input parameters (cq. Eq. (5)), which are related to the hypothesised nature-based solutions displayed on the M, Fr_f -space by Geyer and MacCready (2014) with the same class-labels as in Fig. 2.

5. Discussion

Before discussing the presented results, the discussion reflects on the abilities and limits of the simulation strategy and the study in general

(Section 5.1). Subsequently, the results are discussed by interpreting their physical meaning and relevance (Section 5.2); and translating these findings to the implications for nature-based solutions to mitigate salt intrusion (Section 5.3).

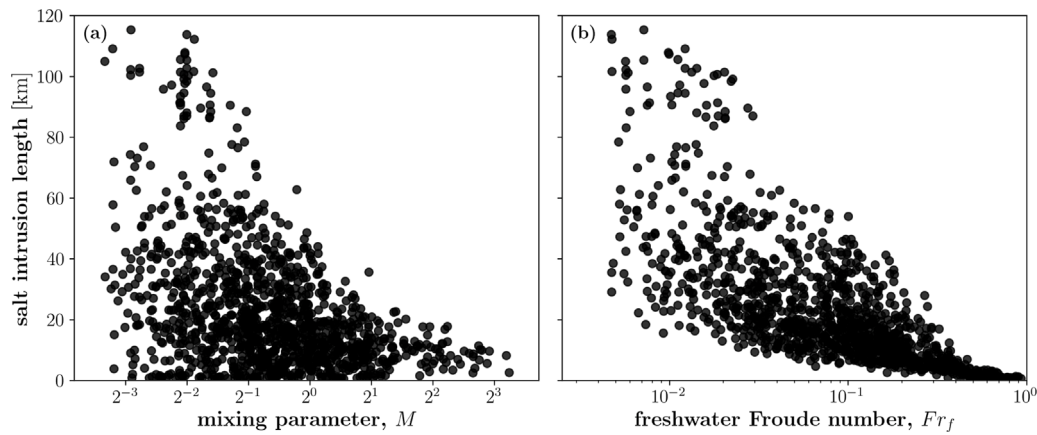


Fig. 7. Simulated salt intrusion length as function of (a) the mixing parameter, M , and (b) the freshwater Froude number, Fr_f .

5.1. Simulation strategy

The implemented method allows for exploring a wide range of possible estuary configurations covering many estuary classes (Fig. 2). However, the many input parameters complicate analyses due to the interaction effects that may obscure single-parameter trends. Nevertheless, clear correlations are visible between various input parameters and the salt intrusion length, e.g., the channel depth and convergence in Fig. 3. We have implemented various analysis methods to contribute to a general understanding of the system, where especially the neural network provides an easy-accessible tool to determine changes in salt intrusion due to modifications in the estuary.

The choice for an idealised model schematisation implies that the model results could not be calibrated or validated against real data. The absolute values should therefore be considered as estimates. However, given the predictive capacity of the 3D process-based modelling software, we assume that the model correctly represents the governing physics. Resulting values form a physical sound basis for the sensitivity analysis of this study, i.e., changes to various estuary scale parameters. The calibration parameters were kept constant throughout, which diminishes their influence on the results when analysed in comparison to each other.

Nevertheless, the implementation of a storm surge—represented by a temporary rise in water level (similar to Perk et al., 2019)—seems to be too simplified to capture its effect on the salt intrusion. This approach leaves out the surface shear stress induced by the wind over the whole domain, which would add landward momentum of the saline, offshore waters.

5.2. Physical interpretation

The non-dimensional space suggested by Geyer and MacCready (2014) to classify estuaries largely explains the variability in salt intrusion length (Fig. 2), where the salt intrusion length is suppressed for larger values of the mixing parameter (M) and/or the freshwater Froude number (Fr_f). This principle is explicated in Fig. 7, where larger values of both non-dimensional parameters put a limit on the maximum salt intrusion length.

The correlations shown in Figs. 2 and 7 between the non-dimensional parameters and the salt intrusion length suggest that the input parameters used in the calculation of M and Fr_f (Eqs. (1) and (2)) largely control the variability in the salt intrusion length. This is in part supported by the results presented in Fig. 4 in which the regression coefficients are displayed. Especially the input parameters that define the freshwater Froude number (Eq. (2)) light up in Fig. 4. The effect of the mixing parameter (Fig. 7a) is weaker than that of the freshwater Froude number and seems to be dominated by the channel depth, as

the tidal range and channel friction are of less relevance according to Fig. 4. That the channel depth and river discharge are of importance to the salt intrusion is not surprising, as analytical relations have been developed that relate the salt intrusion length to primarily the water depth and river discharge (e.g., Hansen and Rattray, 1965; Monismith et al., 2002; Savenije, 1993). In such relations, the tidal influence on the salt intrusion is often reflected by means of a diffusion coefficient (e.g., Gong and Shen, 2011; Monismith et al., 2002).

5.2.1. Tidal damping

Our results show that other input parameters not represented in the M, Fr_f -space are relevant for the determination of the salt intrusion length as well. Fig. 4 highlights the importance of the convergence of the estuary, which is supported by Fig. 3b and in line with the findings of Wei et al. (2017).

The influence of the convergence on the salt intrusion length is twofold: (1) the convergence, in combination with the bottom friction, strongly influences the propagation of the tidal wave (e.g., Friedrichs and Aubrey, 1994; Hunt, 1964; Prandle and Rahman, 1980) and thereby the tidal mixing capacity in the estuary; and (2) the width – and thereby the cross-sectional area – over the estuary is determined based on the convergence, which causes the local fluvial flow velocity to change.

The joint effect of the convergence and channel friction on the tide is encapsulated by a tidal damping coefficient (van Rijn, 2011):

$$\delta = \frac{1}{2} \left(\frac{f}{c_t} - \gamma \right) \quad (7)$$

with

$$f = \frac{8}{3\pi} \frac{gn_c^2 u_t}{d_c^{4/3}}$$

$$c_t = \sqrt{gd_c}$$

where f is a friction parameter [s^{-1}]; c_t the frictionless tidal wave celerity [ms^{-1}]; γ the convergence (Table 1) [m^{-1}]; u_t the tidal velocity [ms^{-1}], similarly defined as for the mixing parameter (M , Eq. (1)). Note that the damping coefficient is positive when the tidal range is damped, and negative when the tide is amplified; i.e., the tidal damping coefficient describes the tidal propagation by the following exponential decay function:

$$a(x) = a_0 \exp[-\delta x]$$

where a_0 is the tidal range at the mouth of the estuary [m].

Fig. 8 presents the salt intrusion length as function of the tidal damping coefficient (Eq. (7)) in two ways: (1) derived from the raw data (black points); and (2) derived from estimates by the neural network exploring the whole (relevant) input space (grey dots). This

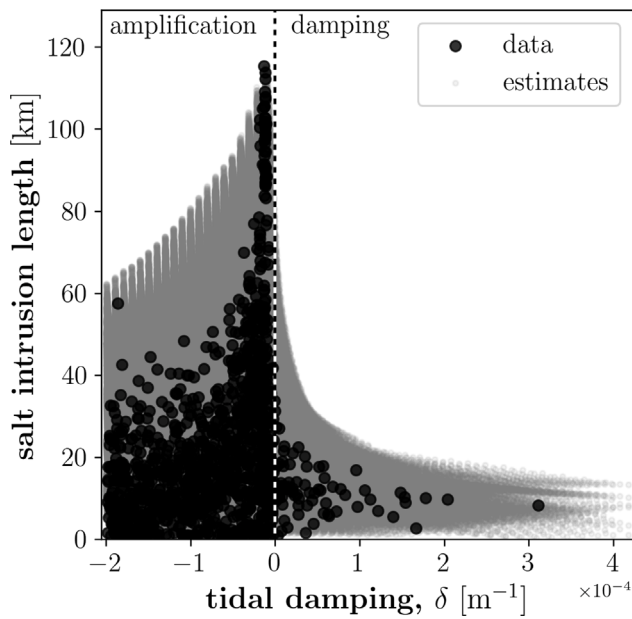


Fig. 8. Salt intrusion length as function of the tidal damping coefficient (Eq. (7)). A negative damping coefficient reflects tidal amplification. Black points represent the results derived from the raw data; and the grey dots the estimates by the neural network.

addition of estimates by the neural network to the raw data is also used in subsequent figures (Figs. 9 to 11) to fill the sparsely sampled input space.

Fig. 8 shows the suppression of the salt intrusion length by the tidal damping coefficient, where the largest salt intrusion occurs around the tipping point between amplification and damping, i.e., $\delta = 0$. This is representative for an “ideal estuary” in which the tidal range and velocity remain spatially constant due to the balancing forces of amplification by convergence and damping by friction (e.g., Dronkers, 2017; Savenije and Velting, 2005).

The reason the salt intrusion peaks when the convergence and friction are in balance follows from the dual effect of the tide on the salt intrusion: On the one hand, the tidal energy mixes the water column reducing the gravitational circulation; on the other hand, the tidal momentum increases the landward reach of the saline water. Thus the maximum salt intrusion can be achieved when there is sufficient tidal momentum pushing the saline water upstream but not enough to reduce the stratification and the gravitational circulation.

However, the effects of a damped or amplified system are not symmetrical as the amplification of the tide results in a larger salt intrusion length compared to a dampened system. This suggests that the tide enforces an upper bound on the salt intrusion length, which is in line with the regression coefficients related to the tidal range in Fig. 4 showing a negative relation between the tidal range and the salt intrusion length.

The non-monotonic response of the salt intrusion length to the damping coefficient as presented in Fig. 8 is also in line with the partial derivative with respect to the channel friction, which has both a positive and negative sign (Fig. 6b), illustrative for the change in salt intrusion length for increasing value of the tidal damping coefficient (Fig. 8).

5.2.2. Tidal asymmetry

The tide and its influence on the salt intrusion length is also influenced by the tidal asymmetry of the estuary (Cheng et al., 2013; Pein et al., 2018). In Section 2, three aspects were introduced that modify the tidal asymmetry of an estuary: (1) tidal flats (Friedrichs and Aubrey, 1988), (2) tidal range to water depth ratio (Friedrichs and Madsen,

1992), and (3) river over tidal flux (Nidzioko and Ralston, 2012). To analyse their effects on the salt intrusion length, three ratios have been defined:

1. The ratio of the bank-full cross-sectional areas of the tidal flats over the channel:

$$\alpha = \frac{\frac{1}{2}a(r_d + 1)W_f}{\left(d_c + \frac{1}{2}a\right)W_c} \quad (8)$$

2. The ratio of the tidal range over the water depth—i.e., channel depth:

$$\Gamma = \frac{a}{d_c} \quad (9)$$

3. The ratio of the river flux over the tidal flux:

$$\varphi = \frac{Q}{2P/T} \quad (10)$$

where P is the tidal prism [m^3], as defined by van Rijn (2011); and T the tidal period [$T = 43,200$ s].

Although these three ratios do not solely encompass the effects of ebb-dominance, a larger value represents an increase of ebb-dominance of the system.

The effects of these ratios on the salt intrusion length are presented in Fig. 9. These results support the statement of a reduction in salt intrusion length for increased ebb-dominance. Again, these three ratios – and thereby the ebb-dominance – impose an upper limit on the salt intrusion length.

The effects of the tidal ratio, Γ , on the salt intrusion length are stronger than the mixing parameter (Fig. 7a) even though the mixing parameter (M , Eq. (1)) embeds the tidal ratio (Γ , Eq. (9)): $M \propto \Gamma d_c^{-5/12} n_c$. This suggests that the effect of the mixing parameter on the salt intrusion length is dominated by the tidal ratio.

5.2.3. Lateral circulation

The meandering of the estuary is described by two input parameters, namely the meander amplitude (A_m) and the meander length (L_m). This complicates the analysis of the effects of meandering on the salt intrusion length. Therefore, the sinuosity of the estuary is considered, which describes the degree of meandering and is composed of both the meander amplitude and length:

$$S = \frac{1}{L_m} \int_0^{L_m} \sqrt{1 + \left(\frac{dy}{dx}\right)^2} dx \quad (11)$$

with

$$y(x) = A_m \sin \left[\frac{2\pi}{L_m} x \right]$$

where y is the centre-line of the estuary [m]; and x the longitudinal coordinate [m]. Note that a straight estuary has $S = 1$ and the introduction of meanders results in $S > 1$.

Fig. 10 shows a minor effect of the sinuosity on the salt intrusion when analysing the simulated samples, which is contradictory to the findings by Pein et al. (2018). However, when the estimates of the neural network covering the whole input space are considered, there seems to be no distinct relation between the sinuosity and the salt intrusion length.

The differences found between the study by Pein et al. (2018) and the results shown in Fig. 10 can be explained by the method used to introduce meanders to the estuary: In Pein et al. (2018), a straight estuary has three bends in the region of maximum salt intrusion—where it has the most influence on the salt intrusion; we applied the meanders throughout the estuary. Furthermore, Pein et al. (2018) state that the length of the estuary remains the same even with the addition of meanders, while we follow the centre-line of the estuary when

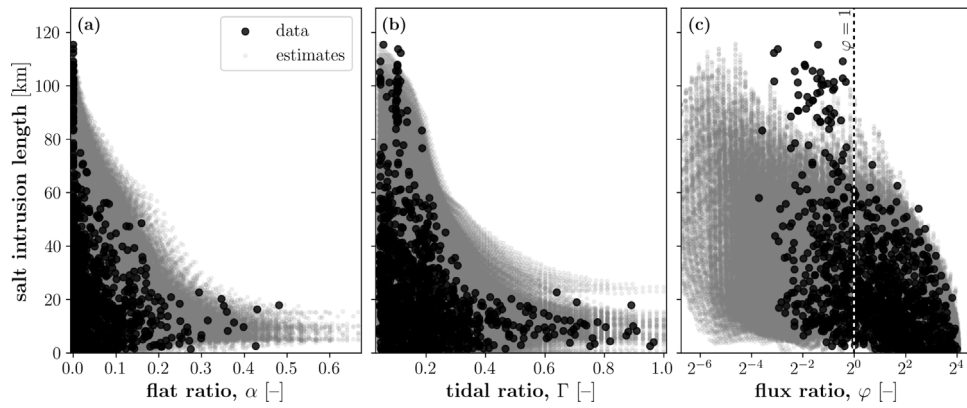


Fig. 9. Salt intrusion length as function of (a) the flat ratio (α , Eq. (8)), (b) the tidal ratio (Γ , Eq. (9)), and (c) the flux ratio (φ , Eq. (10)). Black points represents the results derived from the raw data; and the grey dots the estimates by the neural network.

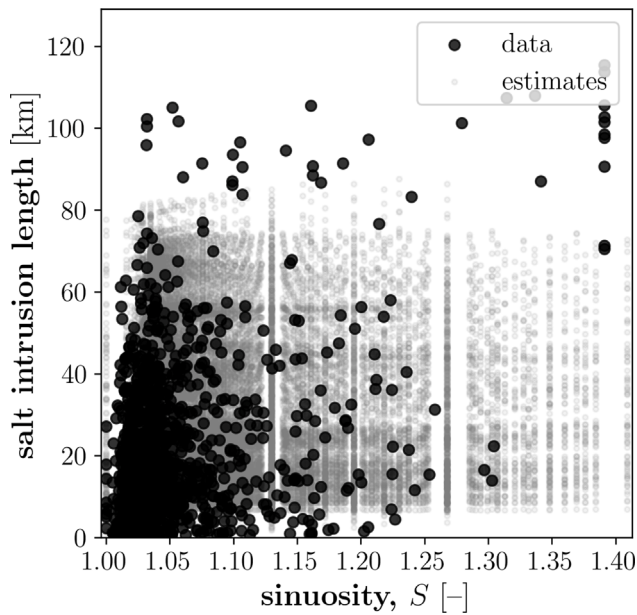


Fig. 10. Salt intrusion length as function of the sinuosity (S , Eq. (11)). Black points represent the results derived from the raw data; and the grey dots the estimates by the neural network.

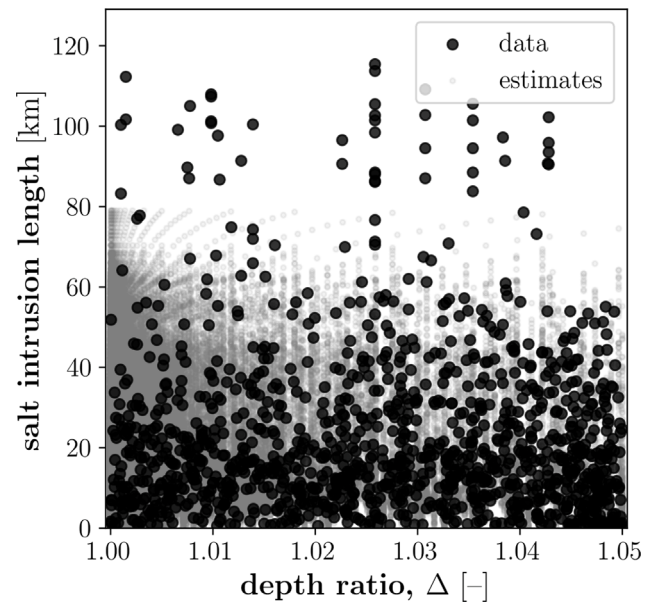


Fig. 11. Salt intrusion length as function of the depth ratio (Δ , Eq. (12)). Black points represent the results derived from the raw data; and the grey dots the estimates by the neural network.

defining the salt intrusion length. If meanders in our simulations do not lead to shortening of the salt intrusion length – measured along the thalweg of the estuary – they will still lead to a shortening in Cartesian space, more or less in proportion to the effective length increase they cause.

The effects of bottom curvature on the salt intrusion length are considered as the relative increase in channel depth in the centre of the estuary, defined as a depth ratio:

$$\Delta = \frac{d_c + \Delta d_c}{d_c} \quad (12)$$

with

$$\Delta d_c = \frac{1}{12} \kappa_c W_c^2$$

where Δd_c is the additional depth along the estuarine centre line [m]. Note that Δd_c averaged over the lateral axis equals zero and thus that the channel depth (d_c) reflects the laterally averaged channel depth.

This relation is displayed in Fig. 11 from which no clear relation can be drawn, similar to the effect of meandering (Fig. 10). Despite

the strong relation between the salt intrusion length and the channel depth, the enhancement of the maximum channel depth caused by the bottom curvature – albeit small – does not follow this pattern. Furthermore, the hypothesised enhanced salt intrusion due to the lateral circulation (Burchard et al., 2011) is also not deducible from Fig. 11.

The absence of a clear relation between the salt intrusion and both the meandering (Fig. 10) and the bottom curvature (Fig. 11) raises the question how relevant the lateral circulation patterns are with respect to the other considered estuary-scale modifications. On the other hand, the interactions between the meandering characteristics and the bottom curvature are highlighted in Fig. 4, which indicates a substantial sensitivity of the salt intrusion length to these first-order interaction terms. However, this relevance is not apparent from correlation plots showcasing these first-order interactions.

This distorted image might be the cause of how the bottom curvature is scaled, where its distribution hints towards a log-based scaling instead of a linear-scaling. Because the input parameters are normalised with the *zero mean, unit variance*-method (Section 3.4.1) and the fact that the bottom curvature is very skewed towards lower values, this might cause discrepancies in the sensitivities.

Another potential cause – which would also reflect upon the meandering characteristics – is the strong correlation between these three input parameters and the channel width (Fig. 4). This seems more reasonable due to the fact that there is a clear (positive) relation between the salt intrusion and the channel width.

Re-scaling of the input parameters to account for the imposed physical restrictions – leading to uncorrelated parameters – removed some of the interactions in the linear model but did not change the nature of the relations with salt intrusion length (results not shown).

At last, it is important to note that the Coriolis effect has not been included in this study. This could, however, have a substantial influence on the lateral circulation patterns (e.g., Cheng et al., 2017) as well as on the salt intrusion length (e.g., Wei et al., 2017).

5.3. Nature-based solutions

In this section, the results and their physical reflections are translated to the hypothesised nature-based solutions (Section 2).

As expected, the reduction of the cross-section greatly reduces the salt intrusion length, as illustrated by Figs. 3 and 4. Although the channel depth is a more effective measure than the width (Fig. 4) and explains a large part of the variation in salt intrusion length, it is a difficult parameter to use as a basis of nature-based solutions. In many estuaries, water depth is maintained at a deeper level than its equilibrium value to accommodate access of large vessels to port areas. Various possibilities might exist to reconcile nature-based solutions to mitigate salt intrusion with harbour access, but the current study does not allow to evaluate these possibilities. One option could be to reduce the depth in a non-uniform way in space (e.g., just behind or around harbour access points). Therefore, focusing on the width instead of the depth in reducing the cross-sectional area could provide a more viable solution to mitigate salt intrusion. In this respect, Fig. 4 suggests that manipulating the width is less effective than manipulating the depth, but that the interaction between both is minimal and as a consequence, the two measures to change the cross-sectional area can be considered complimentary. However, manipulating the depth is likely more effective because it also influences the stratification and mixing in the estuary.

The friction in the estuary competes with the tidal amplification effect of the convergence (Eq. (7)). Fig. 8 highlights the importance of the balance between tidal damping and amplification. The evaluated values of the bottom friction are representative for natural bottom covers. However, the effective bottom friction can be further enhanced by (1) artificially enhancing the bottom friction, e.g., by means of large boulders or even rocks on the bottom; and (2) naturally occurring bed forms, such as ripples and sand waves. The implementation of vegetation at the bottom of the channel might not be suitable in practice, as for vegetation to sustain, light must reach the vegetation, which poses a substantial constraint on the water depth; and submerged vegetation in practice is limited to areas with low current velocity. In addition, ship propellers may pose problems in intensely used estuaries.

Changing the bottom friction as a nature-based solution will require careful consideration of its interaction with the convergence. As shown in Fig. 8, an increased bottom friction can either reduce or enhance the salt intrusion, depending on whether the tide is amplified or damped. Counterintuitively, smoothening the bed may therefore in some cases also result in less salt intrusion.

The introduction of tidal flats to both sides of the estuarine channel places an upper limit on the salt intrusion length (Fig. 9b). On the other hand, Fig. 6c does not display a uniform picture of the implementation of tidal flats. Analysing both Figs. 6c and 9a, demonstrates the relevance of the water depth on the tidal flats – i.e., the flat depth – for its efficiency to mitigate salt intrusion; this is also illustrated by the comparable values of their regression coefficients in Fig. 4.

The addition of tidal flats has been shown to have many other benefits to an estuarine system, such as wave and surge reduction

and coastline stabilisation (e.g., de Vriend et al., 2015; Temmerman et al., 2013; van Wesenbeeck et al., 2014). Even if the tidal flat friction does not prevent salt intrusion very effectively (Fig. 4), the tidal flats allow for ecological development; e.g., in intensely used and dredged estuaries – such as the Western Scheldt in the Netherlands – tidal flats are the only refuges for benthic life, with deeper channels almost devoid of any organisms (Ysebaert et al., 2003).

From this study, both the lateral depth variation – described by the bottom curvature, κ_c – and the meandering of the estuary have no profound effects on the salt intrusion (Figs. 10 and 11). This might be due to several reasons: (1) these hypothesised nature-based solutions are minor interventions that do not make a significant contribution; (2) the representative input parameters and their ranges do not capture the full potential of these optional nature-based solutions; and/or (3) the representative input parameters are implemented incorrectly in the parametric design. Although a parametric design as implemented in this study comes with the cost of simplifying complex features to fit an idealised setting, our investigations of the data suggest the first: The results do align with the literature concerning the remainder of the input parameters—with the exception of the surge level, which is considered an ill-implementation in the parametric design.

Nevertheless, it is important to discriminate between estuary-wide uniform changes to an estuary – as investigated in this study – and local adaptations of the estuary. The implementation of nature-based solutions can also be considered more in the domain of local modifications, such as the local introduction of meanders as described by Pein et al. (2018). Therefore, we recommend not to discard the hypotheses enhancing the lateral circulations.

At last, the river discharge is a dominant factor for the salt intrusion length (Fig. 4). Therefore, it is noteworthy to pose the potential of river discharge management as an optional nature-based solution to mitigate salt intrusion. This can be realised on two different temporal scales: (1) small-scale by releasing the river water in a pulse-like fashion during a drought, exploiting the nonlinear response of the salt intrusion length to temporal changes in river discharge (e.g., Biemond et al., 2022; Gong and Shen, 2011; Hetland and Geyer, 2004; Monismith, 2017); and (2) large-scale by replenishing freshwater reserves during high river discharges to be released during droughts, in essence smoothening the variability in river discharge.

6. Conclusion

The presented study encompasses an extensive numerical experiment analysing the sensitivity of the salt intrusion length with respect to thirteen estuary-scale parameters. The use of machine learning techniques enabled us to implement a computationally expensive, state-of-the-art hydrodynamic modelling framework for this exploratory study, which would otherwise be computationally infeasible. Three different analysis methods have been implemented to deduce the underlying relations in the 1252 model simulations: (1) analysis of the raw output data; (2) over-fitting a regression model and analysing its regression coefficients; and (3) implementing a neural network to determine gradients in the salt intrusion length with respect to the input parameters.

In general, the non-dimensional space used by Geyer and MacCready (2014) to classify estuaries (M and Fr_f , Eqs. (1) and (2), resp.) largely determine the response of the estuary (Figs. 2 and 7), and thereby the five input parameters of which they are composed of are considered essential estuarine characteristics: tidal range, river discharge, (channel) depth, (channel) width, and (channel) friction. In addition, our results show that the convergence of an estuary (Figs. 3b and 8) and the presence of tidal flats (Fig. 9a) should also be considered as essential parameters in determining the extent of the salt intrusion length in estuaries.

The key finding of this study is the capping relation between an input parameter – or combination of input parameters – and the salt

Table 2

Qualitative scoring of the hypothesised nature-based solutions including the relevant input parameters. The scores range from insignificant (\pm) to high potential ($++$). Input parameters included between brackets show additional relevant parameters for the hypotheses.

Hypothesis	Parameter(s)	Score
reduced cross-section	d_c, W_c	++
increased bottom friction	$n_c (n_f, \gamma)$	+
enlarged tidal flats	$r_d, W_f (a)$	+
reduced lateral depth variation	κ_c	\pm
increased meandering	A_m, L_m	\pm
managed river discharge	Q	++

intrusion length, which is indicative of a complex relation between the estuarine response and its characteristics. In other words, favourable settings for large salt intrusion for a single parameter (e.g., large channel depth) is not enough to guarantee this will occur; in most cases, smaller intrusion lengths are observed (Fig. 3a). It is the complex interplay of different estuarine characteristics that determine whether a maximum intrusion event occurs, and how often. This yields a promising perspective towards the development of (nature-based) solutions to mitigate salt intrusion, as it indicates that large salt intrusion lengths are the exception and the result of a combination of unfavourable estuarine characteristics. Therefore, modifying one of the relevant characteristics will mitigate the salt intrusion in the estuary, which allows for flexibility in the choice and implementation of (nature-based) solutions.

Reflecting back on the hypothesised nature-based solutions, Table 2 shows an overview of the effectiveness of mitigating salt intrusion for all hypothesised nature-based solutions. As elaborated on in Section 5, four of the six posed hypotheses show potential to mitigate salt intrusion. This leaves two hypotheses unfit for salt intrusion mitigation: (1) the reduced lateral depth variation; and (2) the meandering estuary. Their relevance in mitigating salt intrusion has been shown in this study to be non-existing—or at best minor (Figs. 10 and 11).

The reduced water depth can be combined with reducing the width, as they both reduce the cross-sectional area through which the river discharge has to flow, enhancing the relative river flow velocity compared to the available river discharge. In this way, the freshwater Froude number (Fr_f , Eq. (2)) is enlarged, which has a capping effect on the salt intrusion length (Fig. 7b). Thereby, modifying the cross-sectional area mainly acts to enhance the flushing by river flow. A major question for this type of solutions is whether they can be morphologically stable. If a restriction is added to an otherwise broad and deep estuary, the sediment restricting the flow locally will be subject to increased flow velocities and become unstable. In many cases, however, it is possible to stop – or reduce – dredging in order to reduce the depth, and those solutions appear stable from a physical perspective.

The bottom friction in combination with the convergence modify the tidal wave in the estuary. The bottom friction enhances the tidal mixing (M , Eq. (1)) and the tidal damping (Eq. (7)); and the convergence amplifies the tidal wave in the estuary (Eq. (7)) concentrating the tidal energy over a smaller cross-sectional area for enhanced mixing. Here, the bottom friction in the channel is relevant, while the bottom friction on the tidal flats is of no importance in the mitigation of salt intrusion.

The presence of tidal flats is relevant in mitigating salt intrusion (Fig. 9a). This is not so much due to the friction they impose, but rather due to their water storage and effect on tidal asymmetry. The irrelevance of the flat friction allows for variety in ecological development on these flats, creating system-specific additional value to the system; an important component of the *Building with Nature*-philosophy (e.g., de Vriend et al., 2015; van Slobbe et al., 2013).

Although boundary conditions are harder to influence compared to the geomorphological features of an estuary, the fluctuations in river discharge due to the seasons can be smoothed to reduce the fluctuations in salt intrusion over the year. This would provide a more

constant and reliable salt distribution in an estuary, which makes spatial planning easier.

All in all, there are clear – albeit sometimes quite complex – correlations between (a combination of) estuary-scale parameters and the salt intrusion length in an estuary. These relations all describe a capping behaviour of the salt intrusion length. Thus, unfavourable characteristics do not necessarily result in a large salt intrusion length as long as one dominant characteristic suppresses the salt intrusion. This behaviour is ideal for the development and implementation of (nature-based) solutions to mitigate salt intrusion.

Software availability

The trained and implemented neural network is open-access and named ANNESI (Artificial Neural Network for Estuarine Salt Intrusion; Hendrickx, 2022).

CRedit authorship contribution statement

Gijs G. Hendrickx: Writing – review & editing, Writing – original draft, Visualization, Methodology, Investigation, Formal analysis, Data curation, Conceptualization. **Wouter M. Kranenburg:** Writing – review & editing, Formal analysis. **José A.A. Antolínez:** Writing – review & editing, Methodology. **Ymkje Huismans:** Writing – review & editing, Formal analysis. **Stefan G.J. Aarninkhof:** Writing – review & editing, Conceptualization. **Peter M.J. Herman:** Writing – review & editing, Methodology, Formal analysis, Conceptualization.

Declaration of competing interest

The authors declare that they have no known competing financial interests or personal relationships that could have appeared to influence the work reported in this paper.

Data availability

The dataset used in this study is publicly available as NEESI: Numerical Experiments of Estuarine Salt Intrusion dataset (Hendrickx, 2023).

Acknowledgements

We are indebted to Ariana Torres (SURF) for her support in the development of the computational manager for the many simulations executed. This work used the Dutch national e-infrastructure with the support of the SURF Cooperative, The Netherlands using grant no. EINF-1548. At last, we would also like to thank the three anonymous reviewers for their valuable feedback on the original manuscript; there suggestions greatly improved the manuscript.

Funding

This publication is part of the project “Design and operation of nature-based SALTISolutions” (with project number P18-32 Project 7) of the research programme SALTISolutions which is (partly) financed by the Dutch Research Council (NWO).

Appendix A. Supplementary data

Supplementary material related to this article can be found online at <https://doi.org/10.1016/j.ecss.2023.108564>.

References

- Biamond, B., de Swart, H.E., Dijkstra, H.A., Díez-Minguito, M., 2022. Estuarine salinity response to freshwater pulses. *J. Geophys. Res.: Oceans* 127 (11), 1–18. <http://dx.doi.org/10.1029/2022JC018666>.
- Borsje, B.W., van Wesenbeeck, B.K., Dekker, F., Paalvast, P., Bouma, T.J., van Katwijk, M.M., de Vries, M.B., 2011. How ecological engineering can serve in coastal protection. *Ecol. Eng.* 37 (2), 113–122. <http://dx.doi.org/10.1016/j.ecoleng.2010.11.027>, URL <https://linkinghub.elsevier.com/retrieve/pii/S0925857410003216>.
- Burchard, H., Hetland, R.D., 2010. Quantifying the contributions of tidal straining and gravitational circulation to residual circulation in periodically stratified tidal estuaries. *J. Phys. Oceanogr.* 40 (6), 1243–1262. <http://dx.doi.org/10.1175/2010JPO4270.1>, URL http://journals.ametsoc.org/jpo/article-pdf/40/6/1243/4514077/2010jpo4270_1.pdf.
- Burchard, H., Hetland, R.D., Schulz, E., Schuttelaars, H.M., 2011. Drivers of residual estuarine circulation in tidally energetic estuaries: Straight and irrotational channels with parabolic cross section. *J. Phys. Oceanogr.* 41 (3), 548–570. <http://dx.doi.org/10.1175/2010JPO4453.1>, URL http://journals.ametsoc.org/jpo/article-pdf/41/3/548/4516178/2010jpo4453_1.pdf.
- Chant, R.J., Sommerfield, C.K., Talke, S.A., 2018. Impact of channel deepening on tidal and gravitational circulation in a highly engineered estuarine basin. *Estuaries Coasts* 41 (6), 1587–1600. <http://dx.doi.org/10.1007/s12237-018-0379-6>, URL <https://link.springer.com/article/10.1007/s12237-018-0379-6>.
- Cheng, P., de Swart, H.E., Valle-Levinson, A., 2013. Role of asymmetric tidal mixing in the subtidal dynamics of narrow estuaries. *J. Geophys. Res.: Oceans* 118 (5), 2623–2639. <http://dx.doi.org/10.1002/jgrc.20189>, URL <http://doi.wiley.com/10.1002/jgrc.20189>.
- Cheng, P., Valle-Levinson, A., de Swart, H.E., 2010. Residual currents induced by asymmetric tidal mixing in weakly stratified narrow estuaries. *J. Phys. Oceanogr.* 40 (9), 2135–2147. <http://dx.doi.org/10.1175/2010JPO4314.1>, URL http://journals.ametsoc.org/jpo/article-pdf/40/9/2135/4510476/2010jpo4314_1.pdf.
- Cheng, P., Wang, A., Jia, J., 2017. Analytical study of lateral-circulation-induced exchange flow in tidally dominated well-mixed estuaries. *Cont. Shelf Res.* 140, 1–10. <http://dx.doi.org/10.1016/j.csr.2017.03.013>.
- Costall, A., Harris, B., Pigois, J.P., 2018. Electrical resistivity imaging and the saline water interface in high-quality coastal aquifers. *Surv. Geophys.* 39 (4), 753–816. <http://dx.doi.org/10.1007/s10712-018-9468-0>, URL <https://link.springer.com/article/10.1007/s10712-018-9468-0>.
- de Vriend, H.J., van Koningsveld, M., Aarninkhof, S.G.J., de Vries, M.B., Baptist, M.J., 2015. Sustainable hydraulic engineering through Building with Nature. *J. Hydro-Environ. Res.* 9 (2), 159–171. <http://dx.doi.org/10.1016/j.jher.2014.06.004>, URL <https://www.sciencedirect.com/science/article/pii/S1570644314000653>.
- Dijkstra, Y.M., Schuttelaars, H.M., 2021. A unifying approach to subtidal salt intrusion modeling in tidal estuaries. *J. Phys. Oceanogr.* 51 (1), 147–167. <http://dx.doi.org/10.1175/jpo-d-20-0006.1>.
- Distefano, T., Kelly, S., 2017. Are we in deep water? Water scarcity and its limits to economic growth. *Ecol. Econom.* 142, 130–147. <http://dx.doi.org/10.1016/j.ecolecon.2017.06.019>.
- Dronkers, J., 2017. Convergence of estuarine channels. *Cont. Shelf Res.* 144, 120–133. <http://dx.doi.org/10.1016/j.csr.2017.06.012>.
- Fischer, H.B., List, E.J., Koh, R.C.Y., Imberger, J., Brooks, N.H., 1979. *Mixing in Inland and Coastal Waters*. Academic Press, <http://dx.doi.org/10.1016/C2009-0-22051-4>, URL <https://www.sciencedirect.com/book/9780080511771/mixing-in-inland-and-coastal-waters{#}book-info>.
- Friedrichs, C.T., Aubrey, D.G., 1988. Non-linear tidal distortion in shallow well-mixed estuaries: A synthesis. *Estuar. Coast. Shelf Sci.* 27 (5), 521–545. [http://dx.doi.org/10.1016/0272-7714\(88\)90082-0](http://dx.doi.org/10.1016/0272-7714(88)90082-0).
- Friedrichs, C.T., Aubrey, D.G., 1994. Tidal propagation in strongly convergent channels. *J. Geophys. Res.* 99 (C2), 3321–3336. <http://dx.doi.org/10.1029/93JC03219>.
- Friedrichs, C.T., Madsen, O.S., 1992. Nonlinear diffusion of the tidal signal in frictionally dominated embayments. *J. Geophys. Res.* 97 (C4), 5637. <http://dx.doi.org/10.1029/92jc00354>.
- García, A.M.P., Geyer, W.R., Randall, N., 2021. Exchange flows in tributary creeks enhance dispersion by tidal trapping. *Estuaries Coasts* 45 (2), 363–381. <http://dx.doi.org/10.1007/s12237-021-00969-4>.
- Geyer, W.R., 1997. Influence of wind on dynamics and flushing of shallow estuaries. *Estuar. Coast. Shelf Sci.* 44 (6), 713–722. <http://dx.doi.org/10.1006/ecss.1996.0140>.
- Geyer, W.R., MacCready, P., 2014. The estuarine circulation. *Annu. Rev. Fluid Mech.* 46 (1), 175–197. <http://dx.doi.org/10.1146/annurev-fluid-010313-141302>, <https://www.annualreviews.org/doi/10.1146/annurev-fluid-010313-141302>.
- Gong, W., Shen, J., 2011. The response of salt intrusion to changes in river discharge and tidal mixing during the dry season in the Modaomen Estuary, China. *Cont. Shelf Res.* 31 (7–8), 769–788. <http://dx.doi.org/10.1016/j.csr.2011.01.011>.
- Gramacy, R.B., Lee, H.K.H., 2009. Adaptive design and analysis of supercomputer experiments. *Technometrics* 51 (2), 130–145. <http://dx.doi.org/10.1198/TECH.2009.0015>, [arXiv:0805.4359](https://arxiv.org/abs/0805.4359).
- Hansen, D.V., Rattray, Jr., M., 1965. Gravitational circulation in straits and estuaries. *J. Mar. Res.* 23, 104–122.
- Hendrickx, G.G., 2022. ANNESI: An Open-Source Artificial Neural Network for Estuarine Salt Intrusion. 4TU.ResearchData, <http://dx.doi.org/10.4121/19307693>.
- Hendrickx, G.G., 2023. NEESI: Numerical Experiments of Estuarine Salt Intrusion dataset. 4TU.ResearchData, <http://dx.doi.org/10.4121/22272247>.
- Hendrickx, G.G., Antolínez, J.A.A., Herman, P.M.J., 2023. Predicting the response of complex systems for coastal management. *Coast. Eng.* 182, 104289. <http://dx.doi.org/10.1016/j.coastaleng.2023.104289>.
- Hetland, R.D., Geyer, W.R., 2004. An idealized study of the structure of long, partially mixed estuaries. *J. Phys. Oceanogr.* 34 (12), 2677–2691. <http://dx.doi.org/10.1175/JPO2646.1>.
- Hunt, J.N., 1964. Tidal oscillations in estuaries. *Geophys. J. R. Astron. Soc.* 8 (4), 440–455. <http://dx.doi.org/10.1111/j.1365-246X.1964.tb03863.x>.
- Jay, D.A., Musiak, J.D., 1994. Particle trapping in estuarine tidal flows. *J. Geophys. Res.* 99 (C10), <http://dx.doi.org/10.1029/94jc00971>.
- Kennard, R.W., Stone, L.A., 1969. Computer aided design of experiments. *Technometrics* 11 (1), 137–148. <http://dx.doi.org/10.1080/00401706.1969.10490666>.
- Kernkamp, H.W.J., van Dam, A., Stelling, G.S., de Goede, E.D., 2011. Efficient scheme for the shallow water equations on unstructured grids with application to the Continental Shelf. *Ocean Dyn.* 61 (8), 1175–1188. <http://dx.doi.org/10.1007/s10236-011-0423-6>.
- Kranenburg, W.M., van der Kaaij, T., Tiessen, M., Friocourt, Y., Blaas, M., 2022. Salt intrusion in the Rhine Meuse Delta: Estuarine circulation, tidal dispersion or surge effect. In: *Proceedings of the 39th IAHR World Congress*. June. Granada, Spain, pp. 5601–5608. <http://dx.doi.org/10.3850/iahr-39wc2521711920221058>.
- Kuijper, K., van Rijn, L.C., 2011. Analytical and numerical analysis of tides and salinities in estuaries; Part II: Salinity distributions in prismatic and convergent tidal channels. *Ocean Dyn.* 61 (11), 1743–1765. <http://dx.doi.org/10.1007/s10236-011-0454-z>, URL <https://link.springer.com/article/10.1007/s10236-011-0454-z>.
- Lerczak, J.A., Geyer, W.R., 2004. Modeling the lateral circulation in straight, stratified estuaries. *J. Phys. Oceanogr.* 34 (6), 1410–1428. [http://dx.doi.org/10.1175/1520-0485\(2004\)034<1410:MTLCIS>2.0.CO;2](http://dx.doi.org/10.1175/1520-0485(2004)034<1410:MTLCIS>2.0.CO;2), URL <http://journals.ametsoc.org/jpo/article-pdf/34/6/1410/4470862/1520-0485>.
- Lerczak, J.A., Geyer, W.R., Ralston, D.K., 2009. The temporal response of the length of a partially stratified estuary to changes in river flow and tidal amplitude. *J. Phys. Oceanogr.* 39 (4), 915–933. <http://dx.doi.org/10.1175/2008JPO3933.1>, URL http://journals.ametsoc.org/jpo/article-pdf/39/4/915/4499990/2008jpo3933_1.pdf.
- Leuven, J.R.F.W., van Maanen, B., Lexmond, B.R., van der Hoek, B.V., Spruijt, M.J., Kleinhans, M.G., 2018a. Dimensions of fluvial-tidal meanders: Are they disproportionately large? *Geology* 46 (10), 923–926. <http://dx.doi.org/10.1130/G45144.1>, URL www.gsapubs.org.
- Leuven, J.R.F.W., Pierik, H.J., van der Vegt, M., Bouma, T.J., Kleinhans, M.G., 2019. Sea-level-rise-induced threats depend on the size of tide-influenced estuaries worldwide. *Nature Clim. Change* 9 (12), 986–992. <http://dx.doi.org/10.1038/s41558-019-0608-4>.
- Leuven, J.R.F.W., Verhoeve, S.L., van Dijk, W.M., Selaković, S., Kleinhans, M.G., 2018b. Empirical assessment tool for bathymetry, flow velocity and salinity in estuaries based on tidal amplitude and remotely-sensed imagery. *Remote Sens.* 10 (12), <http://dx.doi.org/10.3390/rs10121915>.
- Lyu, H., Zhu, J., 2019. Impacts of tidal flat reclamation on saltwater intrusion and freshwater resources in the changjiang estuary. *J. Coast. Res.* 35 (2), 314–321. <http://dx.doi.org/10.2112/JCOASTRES-D-18-00077.1>, URL <https://bioone.org/journals/journal-of-coastal-research/volume-35/issue-2/JCOASTRES-D-18-00077.1/Impacts-of-Tidal-Flat-Reclamation-on-Saltwater-Intrusion-and-Freshwater/10.2112/JCOASTRES-D-18-00077.1.full>.
- MacCready, P., 1999. Estuarine adjustment to changes in river flow and tidal mixing. *J. Phys. Oceanogr.* 29 (4), 708–726. [http://dx.doi.org/10.1175/1520-0485\(1999\)029<0708:EATCIR>2.0.CO;2](http://dx.doi.org/10.1175/1520-0485(1999)029<0708:EATCIR>2.0.CO;2).
- MacCready, P., Geyer, W.R., 2010. Advances in estuarine physics. *Ann. Rev. Mar. Sci.* 2 (1), 35–58. <http://dx.doi.org/10.1146/annurev-marine-120308-081015>, URL <http://www.annualreviews.org/doi/10.1146/annurev-marine-120308-081015>.
- Mekonnen, M.M., Hoekstra, A.Y., 2016. Sustainability: Four billion people facing severe water scarcity. *Sci. Adv.* 2 (2), <http://dx.doi.org/10.1126/sciadv.1500323>, URL <https://www.science.org/doi/abs/10.1126/sciadv.1500323>.
- Monismith, S.G., 2017. An integral model of unsteady salinity intrusion in estuaries. *J. Hydraul. Res.* 55 (3), 392–408. <http://dx.doi.org/10.1080/00221686.2016.1274682>, URL <https://www.tandfonline.com/doi/full/10.1080/00221686.2016.1274682>.
- Monismith, S.G., Kimmerer, W., Burau, J.R., Stacey, M.T., 2002. Structure and flow-induced variability of the subtidal salinity field in northern San Francisco Bay. *J. Phys. Oceanogr.* 32 (11), 3003–3019. [http://dx.doi.org/10.1175/1520-0485\(2002\)032<3003:SAFIVO>2.0.CO;2](http://dx.doi.org/10.1175/1520-0485(2002)032<3003:SAFIVO>2.0.CO;2).
- Nidzicko, N.J., Ralston, D.K., 2012. Tidal asymmetry and velocity skew over tidal flats and shallow channels within a macrotidal river delta. *J. Geophys. Res.: Oceans* 117 (3), C03001. <http://dx.doi.org/10.1029/2011JC007384>, URL <http://doi.wiley.com/10.1029/2011JC007384>.
- Nunes, R.A., Simpson, J.H., 1985. Axial convergence in a well-mixed estuary. *Estuar. Coast. Shelf Sci.* 20, 637–649. [http://dx.doi.org/10.1016/0272-7714\(85\)90112-X](http://dx.doi.org/10.1016/0272-7714(85)90112-X).
- Pein, J., Valle-Levinson, A., Stanev, E.V., 2018. Secondary circulation asymmetry in a meandering, partially stratified estuary. *J. Geophys. Res.: Oceans* 123 (3), 1670–1683. <http://dx.doi.org/10.1002/2016JC012623>.

- Perk, L., van Rijn, L.C., Koudstaal, K., Fordeyn, J., 2019. A rational method for the design of sand dike/dune systems at sheltered sites; Wadden Sea coast of Texel, The Netherlands. *J. Mar. Sci. Eng.* 7 (9), 324. <http://dx.doi.org/10.3390/jmse7090324>, <https://www.mdpi.com/2077-1312/7/9/324/htm>.
- Prandle, D., Rahman, M.M., 1980. Tidal response in estuaries. *J. Phys. Oceanogr.* 10, 1552–1573. [http://dx.doi.org/10.1175/1520-0485\(1980\)010<1552:TRIE>2.0.CO;2](http://dx.doi.org/10.1175/1520-0485(1980)010<1552:TRIE>2.0.CO;2).
- Ralston, D.K., Geyer, W.R., 2019. Response to channel deepening of the salinity intrusion, estuarine circulation, and stratification in an urbanized estuary. *J. Geophys. Res.: Oceans* 124 (7), 4784–4802. <http://dx.doi.org/10.1029/2019JC015006>.
- Ralston, D.K., Geyer, W.R., Lerczak, J.A., 2010. Structure, variability, and salt flux in a strongly forced salt wedge estuary. *J. Geophys. Res.: Oceans* 115 (6), C06005. <http://dx.doi.org/10.1029/2009JC005806>.
- Saltelli, A., Ratto, M., Tarantola, S., Campolongo, F., 2006. Sensitivity analysis practices: Strategies for model-based inference. *Reliab. Eng. Syst. Saf.* 91 (10–11), 1109–1125. <http://dx.doi.org/10.1016/j.res.2005.11.014>.
- Savenije, H.H.G., 1989. Salt intrusion model for high-water slack, low-water slack, and mean tide on spread sheet. *J. Hydrol.* 107 (1–4), 9–18. [http://dx.doi.org/10.1016/0022-1694\(89\)90046-2](http://dx.doi.org/10.1016/0022-1694(89)90046-2).
- Savenije, H.H.G., 1993. Predictive model for salt intrusion in estuaries. *J. Hydrol.* 148 (1–4), 203–218. [http://dx.doi.org/10.1016/0022-1694\(93\)90260-G](http://dx.doi.org/10.1016/0022-1694(93)90260-G).
- Savenije, H.H.G., Toffolon, M., Haas, J., Veling, E.J.M., 2008. Analytical description of tidal dynamics in convergent estuaries. *J. Geophys. Res.: Oceans* 113 (10), <http://dx.doi.org/10.1029/2007JC004408>, <https://agupubs.onlinelibrary.wiley.com/doi/full/10.1029/2007JC004408>, <https://agupubs.onlinelibrary.wiley.com/doi/abs/10.1029/2007JC004408>, <https://agupubs.onlinelibrary.wiley.com/doi/10.1029/2007JC004408>.
- Savenije, H.H.G., Veling, E.J.M., 2005. Relation between tidal damping and wave celerity in estuaries. *J. Geophys. Res.: Oceans* 110 (4), 1–10. <http://dx.doi.org/10.1029/2004JC002278>.
- Scheres, B., Schüttrumpf, H., 2019. Enhancing the ecological value of sea dikes. *Water (Switzerland)* 11 (8), 1617. <http://dx.doi.org/10.3390/w11081617>, URL <https://www.mdpi.com/2073-4441/11/8/1617>.
- Simpson, J.H., Brown, J., Matthews, J., Allen, G., 1990. Tidal straining, density currents, and stirring in the control of estuarine stratification. *Estuaries* 13 (2), 125–132. <http://dx.doi.org/10.2307/1351581>, URL <https://link.springer.com/article/10.2307/1351581>.
- Small, C., Nicholls, R.J., 2003. A global analysis of human settlement in coastal zones. *J. Coast. Res.* 19 (3), 584–599, URL <https://about.jstor.org/terms>.
- Sobol', I.M., 2001. Global sensitivity indices for nonlinear mathematical models and their Monte Carlo estimates. *Math. Comput. Simulation* 55 (1–3), 271–280. [http://dx.doi.org/10.1016/S0378-4754\(00\)00270-6](http://dx.doi.org/10.1016/S0378-4754(00)00270-6).
- Stacey, M.T., Fram, J.P., Chow, F.K., 2008. Role of tidally periodic density stratification in the creation of estuarine subtidal circulation. *J. Geophys. Res.: Oceans* 113 (8), <http://dx.doi.org/10.1029/2007JC004581>.
- Stelling, G.S., Van Kester, J.A.T.M., 1994. On the approximation of horizontal gradients in sigma co-ordinates for bathymetry with steep bottom slopes. *Internat. J. Numer. Methods Fluids* 18 (10), 915–935. <http://dx.doi.org/10.1002/flid.1650181003>, <https://onlinelibrary.wiley.com/doi/10.1002/flid.1650181003>.
- Temmerman, S., Meire, P., Bouma, T.J., Herman, P.M.J., Ysebaert, T., De Vriend, H.J., 2013. Ecosystem-based coastal defence in the face of global change. *Nature* 504 (7478), 79–83. <http://dx.doi.org/10.1038/nature12859>.
- van Rijn, L.C., 2011. Analytical and numerical analysis of tides and salinities in estuaries; Part I: Tidal wave propagation in convergent estuaries. *Ocean Dyn.* 61 (11), 1719–1741. <http://dx.doi.org/10.1007/s10236-011-0453-0>, URL <https://link.springer.com/article/10.1007/s10236-011-0453-0>.
- van Slobbe, E., de Vriend, H.J., Aarninkhof, S.G.J., Lulofs, K., de Vries, M.B., Dircke, P., 2013. Building with Nature: In search of resilient storm surge protection strategies. *Nat. Hazards* 65 (1), 947–966. <http://dx.doi.org/10.1007/s11069-012-0342-y>, URL <https://link.springer.com/article/10.1007/s11069-012-0342-y>.
- van Wesenbeeck, B.K., Mulder, J.P.M., Marchand, M., Reed, D.J., de Vries, M.B., de Vriend, H.J., Herman, P.M.J., 2014. Damming deltas: A practice of the past? Towards nature-based flood defenses. *Estuar. Coast. Shelf Sci.* 140, 1–6. <http://dx.doi.org/10.1016/j.ecss.2013.12.031>.
- Veerapaga, N., Shintani, T., Azhikodan, G., Yokoyama, K., 2020. Study on salinity intrusion and mixing types in a conceptual estuary using 3-D hydrodynamic simulation: Effects of length, width, depth, and bathymetry. In: Nguyen, K., Guillou, S., Gourbesville, P., Thiébot, J. (Eds.), *Estuaries and Coastal Zones in Times of Global Change*. Springer Singapore, Singapore, pp. 13–30. http://dx.doi.org/10.1007/978-981-15-2081-5_2.
- Veldkamp, T.I.E., Wada, Y., de Moel, H., Kumm, M., Eisner, S., Aerts, J.C.J.H., Ward, P.J., 2015. Changing mechanism of global water scarcity events: Impacts of socioeconomic changes and inter-annual hydro-climatic variability. *Global Environ. Change* 32, 18–29. <http://dx.doi.org/10.1016/j.gloenvcha.2015.02.011>.
- Wada, Y., van Beek, L.P.H., van Kempen, C.M., Reckman, J.W.T.M., Vasak, S., Bierkens, M.F.P., 2010. Global depletion of groundwater resources. *Geophys. Res. Lett.* 37 (20), <http://dx.doi.org/10.1029/2010GL044571>, <https://onlinelibrary.wiley.com/doi/full/10.1029/2010GL044571>, <https://onlinelibrary.wiley.com/doi/abs/10.1029/2010GL044571>, <https://agupubs.onlinelibrary.wiley.com/doi/10.1029/2010GL044571>.
- Wada, Y., van Beek, L.P.H., Viviroli, D., Dürr, H.H., Weingartner, R., Bierkens, M.F.P., 2011. Global monthly water stress: 2. Water demand and severity of water stress. *Water Resour. Res.* 47 (7), <http://dx.doi.org/10.1029/2010WR009792>, <https://onlinelibrary.wiley.com/doi/full/10.1029/2010WR009792>, <https://onlinelibrary.wiley.com/doi/abs/10.1029/2010WR009792>, <https://agupubs.onlinelibrary.wiley.com/doi/10.1029/2010WR009792>.
- Wang, F., Huang, G.H., Fan, Y., Li, Y.P., 2020. Robust subsampling ANOVA methods for sensitivity analysis of water resource and environmental models. *Water Resour. Manag.* 34 (10), 3199–3217. <http://dx.doi.org/10.1007/s11269-020-02608-2>.
- Warner, J.C., Geyer, W.R., Lerczak, J.A., 2005. Numerical modeling of an estuary: A comprehensive skill assessment. *J. Geophys. Res.: Oceans* 110 (5), 1–13. <http://dx.doi.org/10.1029/2004JC002691>, <https://agupubs.onlinelibrary.wiley.com/doi/full/10.1029/2004JC002691>, <https://agupubs.onlinelibrary.wiley.com/doi/abs/10.1029/2004JC002691>, <https://agupubs.onlinelibrary.wiley.com/doi/10.1029/2004JC002691>.
- Wei, X., Kumar, M., Schuttelaars, H.M., 2017. Three-dimensional salt dynamics in well-mixed estuaries: Influence of estuarine convergence, Coriolis, and bathymetry. *J. Phys. Oceanogr.* 47 (7), 1843–1871. <http://dx.doi.org/10.1175/JPO-D-16-0247.1>.
- Ysebaert, T., Herman, P.M.J., Meire, P., Craeymeersch, J., Verbeek, H., Heip, C.H.R., 2003. Large-scale spatial patterns in estuaries: Estuarine macrobenthic communities in the Schelde estuary, NW Europe. *Estuar. Coast. Shelf Sci.* 57 (1–2), 335–355. [http://dx.doi.org/10.1016/S0272-7714\(02\)00359-1](http://dx.doi.org/10.1016/S0272-7714(02)00359-1).
- Zhou, J., Stacey, M.T., Holleman, R.C., Nuss, E., Senn, D.B., 2020. Numerical investigation of baroclinic channel-shoal interaction in partially stratified estuaries. *J. Geophys. Res.: Oceans* 125, <http://dx.doi.org/10.1029/2020JC016135>, e2020JC016135.